Exact coherent structures in stably-stratified plane Couette flow

D. Olvera & R. R. Kerswell
School of Mathematics, Bristol University, Bristol, BS8 1TW, UK

(Received 21 June 2017)

The existence of exact coherent structures in stably-stratified plane Couette flow (gravity perpendicular to the plates) is investigated over Reynolds-Richardson number (Re-Ri_b) space for a fluid of unit Prandtl number ($Pr = 1$) using a combination of numerical and asymptotic techniques. Two states are repeatedly discovered using edge-tracking - EQ7 and EQ7-1 in the nomenclature of Gibson & Brand (2014) - and found to connect with 2-dimensional convective roll solutions when tracked to negative Ri_b (the Rayleigh-Benard problem with shear). Both these states and Nagata's (1990) original exact solution feel the presence of stable stratification when $Ri_b = O(Re^{-2})$ or equivalently when the Rayleigh number $Ra := -Ri_b Re^2 Pr = O(1)$. This is confirmed via a stratified extension of the Vortex-Wave-Interaction (VWI) theory of Hall & Sherwin (2010). If the stratification is increased further, EQ7 is found to progressively spanwise and cross-stream localise until a second regime is entered at $Ri_b = O(Re^{-2/3})$. This corresponds to a stratified version of the Boundary Reduced Equation (BRE) regime of Deguchi, Hall & Walton (2013). Increasing the stratification further, appears to lead to a third, *ultimate* regime where $Ri_b = O(1)$ in which the flow fully localises in all three directions at the minimal Kolmogorov scale which then corresponds to the Osmidov scale. Implications for the laminar-turbulent boundary in the (Re-Ri_b) plane are briefly discussed.

1. Introduction

Our understanding of transition to turbulence in linearly-stable shear flows such as plane Couette flow (pCf) and pipe flow has experienced a considerable step forward over the last 25 years based upon the realisation that such flows have many alternative *unstable* solutions such as equilibria, travelling waves and periodic states (Nagata 1990; Waleffe 1998; Faisst & Eckhardt 2003; Wedin & Kerswell 2004). These states, which start to populate phase space at some critical Reynolds number and quickly proliferate as the Reynolds number increases, eventually produce a sufficiently tangled structure of stable and unstable manifolds in phase space to act as a scaffold for the observed complex dynamics (Kerswell 2005; Eckhardt et al. 2007; Gibson and Cvitanović 2010; Kawahara et al. 2012). These states (variously referred to as simple invariant solutions or Exact Coherent Structures (ECS)), can either be embedded in the laminar-turbulent boundary (Wang et al. 2007; Duguet et al. 2008) or sit in the basin of attraction of the turbulent state with some buried in the turbulent attractor itself (Kerswell & Tutty 2007; Gibson et al. 2008). As a consequence, properties of the ECS have something to say about how transition is triggered (Viswanath & Cvitanović 2009; Duguet et al. 2010; Pringle et al. 2012), the subsequent transitional process (Itano & Toh 2001; Skufca et al. 2006; Schneider et al. 2007; Mellibovsky et al. 2009) and features of the turbulent state itself

(e.g. Kawahara & Kida (2001); Hof et al. (2004); Viswanath (2007); Gibson et al. (2008); Chandler & Kerswell (2013); Willis et al (2013); Lucas & Kerswell (2015)).

The motivation for this study is to extend these investigations to stably-stratified shear flow which is the generic situation in environmental and geophysical flows (e.g. oceanic flows are almost always stably stratified - Thorpe (2007)). While there has been previous work on unstably-stratified shear flow - Rayleigh-Benard convection with imposed shear (Clever et al. 1977; Clever & Busse 1992), internally-heated shear flow (Generalis & Nagata 2003) or natural convection with imposed shear Hall (2012) - the only work in computing ECS for stable stratification is that of Clever and Busse (1992,2000) who established that Nagata's (1990) now famous first solution in pCf could be continued back to Rayleigh-Benard convection with shear. This lack of attention might well be because stable stratification is perceived as a universally stabilizing influence although this is now appreciated as an oversimplification (Howard & Maslowe 1973; Huppert 1973; Davey & Reid 1977) or because introducing stratification increases the dimension of parameter space from a very manageable 1 (Re, the Reynolds number) to a more daunting 3 (Re, Ri_b and Pr where the bulk Richardson and Prandtl numbers are defined below).

Mathematically, rather than a complication, stratification actually presents an opportunity to embed the now-well-studied problem of pCf into a larger framework which can smoothly connect to the even-more-well-studied problem of Rayleigh-Benard convection. Physically, another interesting aspect of adding further parameters to the problem is the increased dimension of any laminar-boundary in parameter space. Ignoring the Prandtl number (set to unity throughout this study) still leaves 2 parameters and then a 1-dimensional laminar-turbulent boundary as opposed to the 0-dimensional situation in unstratified pCf (e.g. see figure 1 of Deusebio et al. (2015)). Understanding exactly how this boundary behaves for large Re is an important open problem in stratified turbulence which has obvious implications for parametrising turbulence in ocean, atmosphere and climate models. In particular, if $Ri_b^c(Re)$ defines the laminar-turbulent boundary, does Ri_b^c tend to zero or not as $Re \to \infty$? Having an asymptotic regime where the flow is always transitional opens up interesting new opportunities to probe the complex dynamics involved. An obvious place to start addressing this question is to understand where in parameter space ECS exist since they are currently viewed as necessary precursors for turbulent dynamics. This is the focus of the current study.

The plan of the paper is as follows. Section 2 formulates the problem of stratified plane Couette flow and discusses the numerical methods to be used. In §3.1, an initial investigation is described which identifies where the laminar-turbulent boundary is in the (Re, Ri_b) plane for two typical (small box) geometries. §3.2 then describes the results of edge-tracking in a variety of geometries aimed at uncovering new ECS. Two already known, albeit now stratified, ECS are repeatedly found - EQ7 and EQ7-1 in the nomenclature of Gibson & Brand (2014). In §3.3 these are continued around in (Re, Ri_b) parameter space, including into negative Ri_b (unstable stratification), along with Nagata's (1990) first solution in pCf. In §3.4 the behaviour of EQ7 (which is most robust to stable stratification) is examined at large Re. A stratified version of the Vortex-Wave-Interaction asymptotics of Hall & Sherwin (2010) is then discussed for very weak stratification. As the stratification is increased, a second regime is suggested by the numerical solutions which show EQ7 spanwise-localizing and amounts to a stratified version of the Boundary Reduced Equations of Deguchi, Hall & Walton (2013). A third, ultimate regime is also discussed in which the ECS are fully localised. Section 4 provides a final discussion of the results and future directions for further research.

2. Formulation

2.1. *Stratified plane Couette flow*

We consider the usual plane Couette flow set-up of two (horizontal) parallel plates separated by a distance $2h$ with the top plate moving at $U\hat{\mathbf{x}}$ and the bottom plate moving at $-U\hat{\mathbf{x}}$. Dirichlet boundary conditions are imposed on the density field (Armenio & Sarkar 2002; Garcia-Villalba & del Alamo 2011): the fluid density is $\rho_0 - \Delta_\rho$ at the top plate and $\rho_0 + \Delta_\rho$ at the bottom plate (gravity g is normal to the plates and directed downwards from the top plate to the bottom plate). Using the Boussinesq approximation ($\Delta_\rho \ll \rho_0$), the governing equations can be non-dimensionalised using U, h and Δ_ρ to give

$$\frac{\partial \mathbf{u}}{\partial t} + \mathbf{u}\cdot\nabla\mathbf{u} = -\nabla p - Ri_b\,\rho\,\hat{\mathbf{y}} + \frac{1}{Re}\nabla^2\mathbf{u}, \tag{2.1}$$

$$\nabla\cdot\mathbf{u} = 0, \tag{2.2}$$

$$\frac{\partial \rho}{\partial t} + \mathbf{u}\cdot\nabla\rho = \frac{1}{Re\,Pr}\nabla^2\rho \tag{2.3}$$

where the bulk Richardson number Ri_b, Reynolds number Re, and the Prandtl number Pr (always set to 1 in this study) are respectively defined as:

$$Ri_\mathrm{b} := \frac{\Delta_\rho\, g\, h}{\rho_0\, U^2}, \qquad Re := \frac{U\,h}{\nu}, \qquad Pr := \frac{\nu}{\kappa}. \tag{2.4}$$

Here $\mathbf{u} = (u, v, w)$ is the velocity field, κ the thermal diffusivity, the total dimensional density is $\rho_0 + \rho\Delta_\rho$, p is the pressure and ν is the kinematic viscosity. The boundary conditions are then

$$u(x, \pm1, z, t)) = \pm1 \quad \& \quad \rho(x, \pm1, z, t) = \mp1. \tag{2.5}$$

which admit the steady 1D solution

$$\mathbf{u} = y\,\hat{\mathbf{x}} \quad \& \quad \rho = -y. \tag{2.6}$$

The (possibly large) disturbance fields away from this basic state,

$$\hat{\mathbf{u}}(x, y, z, t) = \mathbf{u} - y\,\hat{\mathbf{x}}, \qquad \hat{\rho}(x, y, z, t) = \rho + y, \tag{2.7}$$

conveniently satisfy homogeneous boundary conditions at $y = \pm1$. Periodic boundary conditions are used in both the (x) streamwise and (z) spanwise directions over wavelengths $L_x h$ and $L_z h$ so that the (non-dimensionalised) computational domain is $L_x \times 2 \times L_z$. In this geometry, the system has the following symmetries: shift (streamwise)-&-reflect (spanwise)

$$\mathcal{S} : (u, v, w, p, \rho)(x, y, z) \to (u, v, -w, p, \rho)(x + \tfrac{1}{2}L_x, y, \tfrac{1}{2}L_z - z), \tag{2.8}$$

a rotation of $\pm\pi$ about the z-axis

$$\Omega : (u, v, w, p, \rho)(x, y, z) \to (-u, -v, w, p, -\rho)(-x, -y, z), \tag{2.9}$$

and spanwise reflection

$$\mathcal{Z} : (u, v, w, p, \rho)(x, y, z) \to (u, v, -w, p, \rho)(x, y, -z). \tag{2.10}$$

The kinetic energy of the disturbance (per unit volume) is

$$E_k := \frac{1}{2V}\int_V \hat{\mathbf{u}}^2 \mathrm{d}V \;=\; \frac{1}{2V}\int_V (\mathbf{u} - y\,\hat{\mathbf{x}})^2 \mathrm{d}V \tag{2.11}$$

which is the sum of the kinetic energy associated with each velocity component,

$$E_k^u := \frac{1}{2V}\int_V \hat{u}^2 \mathrm{d}V, \quad E_k^v := \frac{1}{2V}\int_V \hat{v}^2 \mathrm{d}V \quad \text{and} \quad E_k^w := \frac{1}{2V}\int_V \hat{w}^2 \mathrm{d}V. \tag{2.12}$$

The potential energy of the disturbance (per unit volume) is taken to be

$$E_p := \frac{1}{2V}\int_V Ri_b(\rho + y)^2 \mathrm{d}V \tag{2.13}$$

so that total energy (per unit volume) is

$$E := E_k + E_p = (E_k^u + E_k^v + E_k^w) + E_p. \tag{2.14}$$

An important quantity used for characterising states in what follows is the average wall shear stress deviation away from that of the steady 1D solution (2.6) normalised by the wall shear stress of the steady 1D solution (2.6) defined as

$$\Delta := \frac{1}{L_x L_z}\int_0^{L_x}\int_0^{L_z} \left.\frac{\partial u}{\partial y}\right|_{y=1} dx\,dz - 1 = \frac{1}{L_x L_z}\int_0^{L_x}\int_0^{L_z} \left.\frac{\partial \hat{u}}{\partial y}\right|_{y=1} dx\,dz. \tag{2.15}$$

2.2. *Methods*

The governing equations are solved numerically using a parallelized DNS code 'Diablo' (Taylor 2008 and http://www.damtp.cam.ac.uk/user/jrt51/files.html) which uses a third-order mixed Runge-Kutta-Wray/Crank-Nicolson timestepper. The horizontal directions are periodic and treated pseudospectrally, while a second-order finite-difference discretization is used in the cross-stream direction. The resolution used was typically 64 Fourier modes per 2π in x and z and 128 finite difference points in y. If needed, this resolution was doubled to ensure numerical accuracy. Diablo was used for edge-tracking and to isolate ECS (simple solutions of the governing equations) by coupling it to a Newton-Raphson-GMRES algorithm (Viswanath 2007).

Tracing ECS over parameter space (varying Re, Ri_b, L_x, L_z) was done by two complementary approaches: Diablo coupled to a Newton-Raphson-GMRES scheme and a direct Newton-Raphson solver of the governing equations discretized using spectral methods assuming steadiness in an appropriately chosen Galilean frame. The latter approach is much more efficient if the ECS has many spatial symmetries to optimise the discretization which was via Fourier modes in the (homogeneous) streamwise and spanwise directions and one or two spectral elements in the cross-stream direction. The two-spectral element approach was used to improve accuracy around the mid plane of the domain: details are given in Appendix A.

3. Results

3.1. *Laminar-Turbulent Boundary*

To set the scene for this investigation, we first choose some specific geometries and identify the laminar-turbulent boundary in (Re, Ri_b, Pr) parameter space. In this paper $Pr = 1$ throughout to keep this study focussed although dependency with Pr across the range

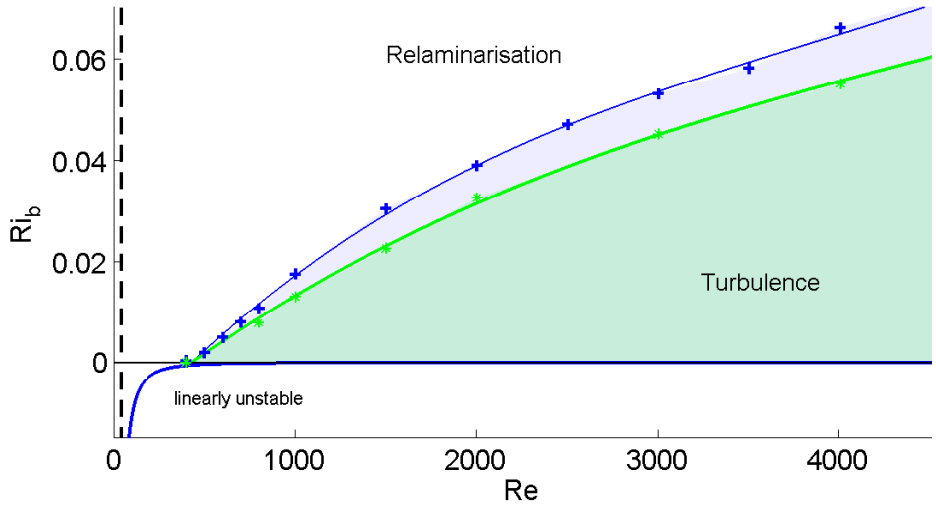

Figure 1: Laminar-turbulent boundary for two geometries $2\pi \times 2 \times 2\pi$ (blue line through the crosses) and $2\pi \times 2 \times \pi$ (green line through the stars). There is linear instability for $Ri_b < -1708/(16Re^2Pr)$ which is the well-known Rayleigh-Benard threshold (unchanged by shear - Kelly (1977)). The energy stability limit is also marked as an (almost) vertical black dashed line.

0.7 (heated air) through 7 (heated water) to 700 (salt in water) is an interesting issue for future examination. A simple protocol was adopted to estimate the position of the laminar-turbulent boundary for the two geometries $2\pi \times 2 \times 2\pi$ and $2\pi \times 2 \times \pi$ and $Re \leq 5000$. At a given point in the parameter plane $(Re, Ri_b, 1)$, 10 simulations were performed with random initial conditions with the point assigned to the turbulent region if 50% or more of these runs remained turbulent after a time $1000\,h/U$ and otherwise to the relaminarisation region. Figure 1 shows that the turbulent part of parameter space extends to higher Ri_b at a given Re for the larger domain with the boundary extending as $Re \to \infty$ for some $Ri_b(Re)$ (see Deusebio et al. (2015) for a similar plot but at higher Re and larger domain size). Also shown for completeness is the region $Ri_b < 0$ (unstable stratification) where the problem is equivalent to Rayleigh-Benard convection with imposed shear: see appendix B which shows how the usual Rayleigh number $Ra = -Ri_b Re^2 Pr$ and the neutral stability line is given by $Ra = 1708/16$ (the extra factor of 16 because the boundary separation has been non-dimensionalised to 2 rather than 1).

Since the laminar-turbulent boundary exists in a 2-dimensional parameter plane, it can be approached in two different ways starting from the turbulent region: either decreasing Re at fixed Ri_b or increasing Ri_b at fixed Re. Work in unstratified flows indicates that the laminar-turbulent boundary (or 'edge' manifold if the turbulence is not strictly an attractor - see Skufca et al. (2006)) and the turbulent attractor collide when turbulence ceases to exist (e.g. figure 5, Schneider & Eckhardt 2009). This type of behaviour carries over to weakly stratified (small Ri_b) shear flow here: the top plots in Figure 2 show the energy levels of the turbulence and edge manifold coming together as Re is decreased towards the boundary. A similar convergence of energy levels also seems to occur for fixed (high) Re and increasing Ri_b (bottom plots of Figure 2), but the dominant feature now is the presence of increasingly large *and* slower fluctuations in the turbulent energy level

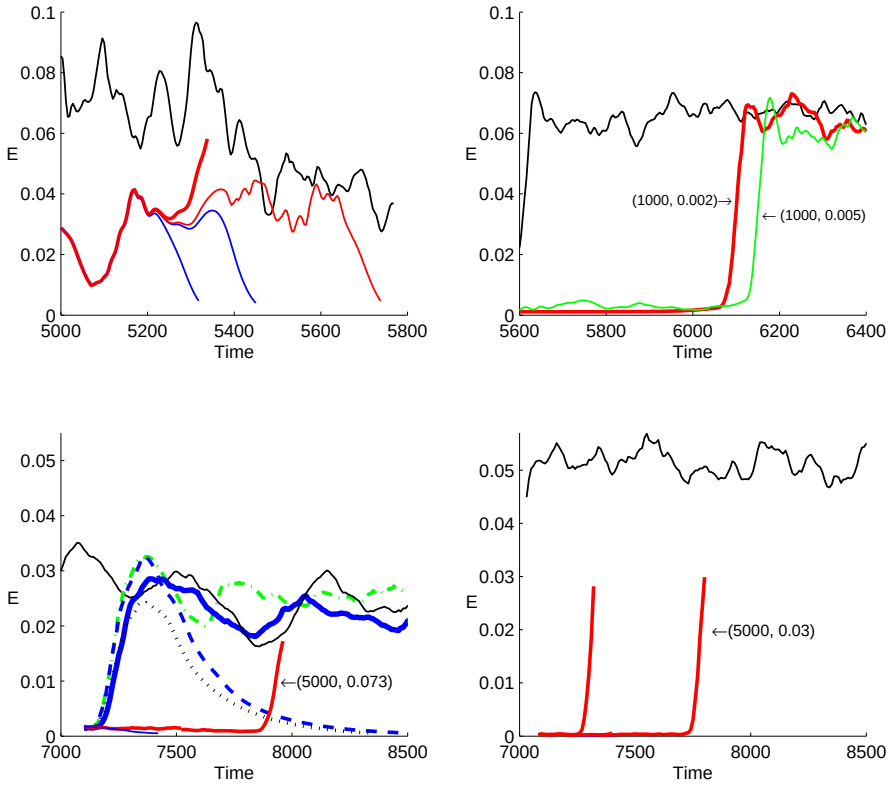

Figure 2: Edge (red, lower, flatter lines) and turbulent (black, upper, jagged lines) kinetic energy levels either receding from the laminar-turbulent boundary at fixed low Ri_b and Re increasing left-to-right (top) or from fixed Re and Ri_b decreasing left-to-right bottom (i.e. left figures are approaching laminar-turbulent interface compared to right figures). Top left $(Re, Ri_b) = (400, 0.002)$; top right $(Re, Ri_b) = (1000, 0.002)$ red, $(Re, Ri_b) = (1000, 0.005)$ green; bottom left $Re = 5000$ and $Ri_b = 0.073$ black, $Ri_b = 0.075$ green dash-dot, $Ri_b = 0.077$ blue dashed, $Ri_b = 0.08$ blue, $Ri_b = 0.085$ black dotted line; bottom right $(Re, Ri_b) = (5000, 0.03)$.

as the boundary is approached. The lines for $Ri_b = 0.077$ (blue dashed) and $Ri_b = 0.08$ (solid blue) in the bottom left plot of figure 2 show how a less-stratified flow can reach the energy levels of the turbulent state yet immediately relaminarise while a more-stratified flow can stay turbulent albeit with large fluctuations in energy. It seems that sustained turbulence is lost in the latter case by the turbulent attractor expanding to touch the edge manifold as opposed to moving as a whole towards it in the former case.

3.2. *Identifying ECS: Edge Tracking*

The method of edge tracking was used to identify ECS (Itano & Toh 2001; Skufca et al. 2006) without any imposed symmetries unless explicitly stated. This method seeks to find attractors on the laminar-turbulent boundary by a bisection approach. The approach can be 'hit or miss' - the attractor may turn out to be chaotic rather than simple (i.e. an equilibrium, travelling wave or periodic state) - but does have the advantage that if

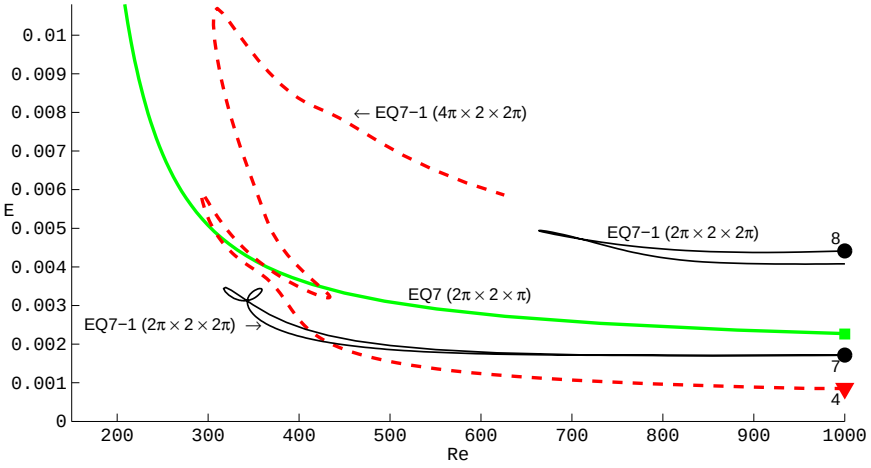

Figure 3: Continuation in Re at $Ri_b = 0$ starting at $Re = 1000$ for EQ7-1 in boxes $4\pi \times 2 \times 2\pi$ (red dashed - - -) and $2\pi \times 2 \times 2\pi$ (thin black —— for both, upper and lower disconnected branches), and continuation for EQ7 in box $2\pi \times 2 \times \pi$ (bold green ——). Points 4, 7 and 8 are marked in the continuation in Ri_b in figure 4.

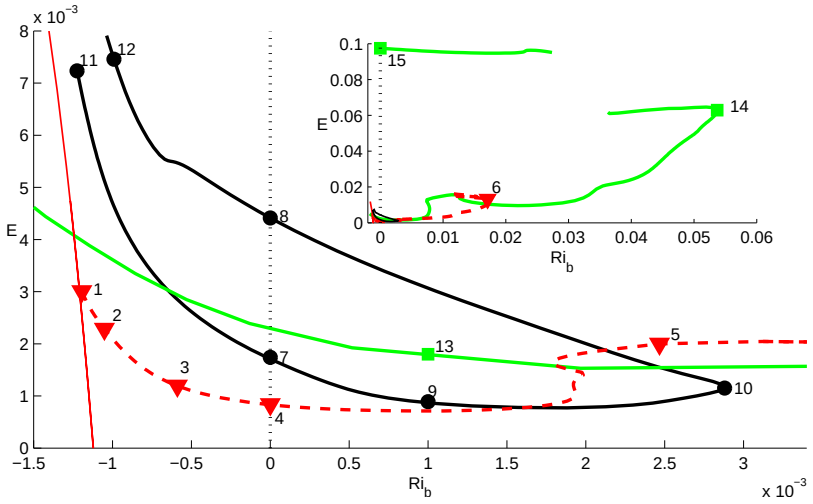

Figure 4: Continuation in Ri_b at $Re = 1000$ for solution EQ7-1 in boxes $4\pi \times 2 \times 2\pi$ (red dashed - - -) and $2\pi \times 2 \times 2\pi$ (bold dark ——), EQ7 in box $2\pi \times 2 \times \pi$ (bold green ——) and 2D Rayleigh-Benard solution in box $4\pi \times 2 \times 2\pi$ (thin red ——). Inset shows how solution EQ7 reaches larger values of stratification close to $Ri_b \sim 0.06$. The curves shown have been traced by continuing from the lower and upper branch solutions in the unstratified situation and cannot obviously be brought together - see §3.3 for more details.

an ECS is found then it is known to help organise the transition process and therefore be dynamically important. Crucially, the method also offers an unbiased approach to finding ECS in contrast to simply taking known ECS at $Ri_b = 0$ and continuing them into the region $Ri_b > 0$. Since adding stable stratification to a shear flow introduces the

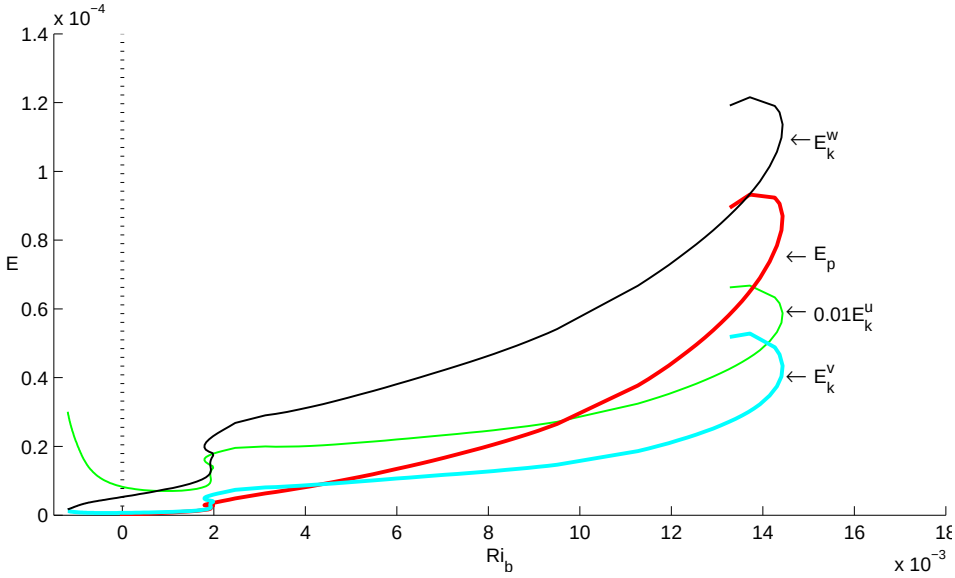

Figure 5: Continuation in Ri_b at $Re = 1000$ for solution EQ7-1 in box $4\pi \times 2 \times 2\pi$. Red dashed line in figure 4. The kinetic energy is splitted into its three components (E_u, E_v and E_w)

additional phenomenon of internal gravity waves, it is possible that new forms of ECS could exist strictly for $Ri_b > 0$. These would have different underpinning dynamics to that in unstratified flows (known variously as the self-sustaining process (SSP) - Waleffe (1995, 1997) or Vortex-Wave-Interaction (VWI) - Hall & Smith (1991); Hall & Sherwin (2010)) and therefore would be of considerable interest.

The investigation was started by reproducing Schneider et al.'s (2008) unstratified edge state calculation for $(Re, Ri_b, L_x, L_z) = (400, 0, 4\pi, 2\pi)$. Adding even a little stratification ($Ri_b = 1 \times 10^{-3}$) moved the system too close to the laminar-turbulent boundary to make edge tracking still feasible (the separation between the edge and the turbulent energy levels becomes too small) so Re was increased to 1000. Here, the unstratified calculation recovers a variant of the edge state at $Re = 400$ (a member of the Nagata (1990) family of solutions) while taking $(Re, Ri_b, L_x, L_z) = (1000, 1 \times 10^{-3}, 4\pi, 2\pi)$ led to a spanwise-localised equilibrium with $\mathcal{S}$ and Ω symmetries. Increasing Ri_b above 1×10^{-3} led to a chaotic edge state so the search was moved to a shorter domain $(Re, Ri_b, L_x, L_z) = (1000, 1 \times 10^{-3}, 2\pi, 2\pi)$ where edge-tracking again revealed a spanwise-localised equilibrium. Branch-continuing this state back to the $4\pi \times 2 \times 2\pi$ box recovered the spanwise-localised state found previously. Continuing this state in the $2\pi \times 2 \times 2\pi$ box from $Ri_b = 1 \times 10^{-3}$ down to 0 and then continuing Re similarly downwards indicated that this spanwise-localised state was the stratified version of EQ7-1 in the nomenclature of Gibson & Brand (2014): compare figure 3 with figure 4 of Gibson & Brand (2014) (note the ordinates are different and we have multiple curves for EQ7-1).

The results of continuing EQ7-1 around in Ri_b at fixed $Re = 1000$ for both geometries is shown in figure 4. In the $4\pi \times 2 \times 2\pi$ box, EQ7-1 exists at Ri_b comparable to that at the laminar-turbulent boundary (see figure 1), while, in the $2\pi \times 2 \times 2\pi$ box, EQ7-1 only reaches to $Ri_b = 2.87 \times 10^{-3}$ before turning back. In the bigger box, figure 5 indicates that at the saddle node point (point of maximum Ri_b) the potential energy of EQ7-1 is almost twice the kinetic energy of the cross-stream (vertical) velocity. At this point the

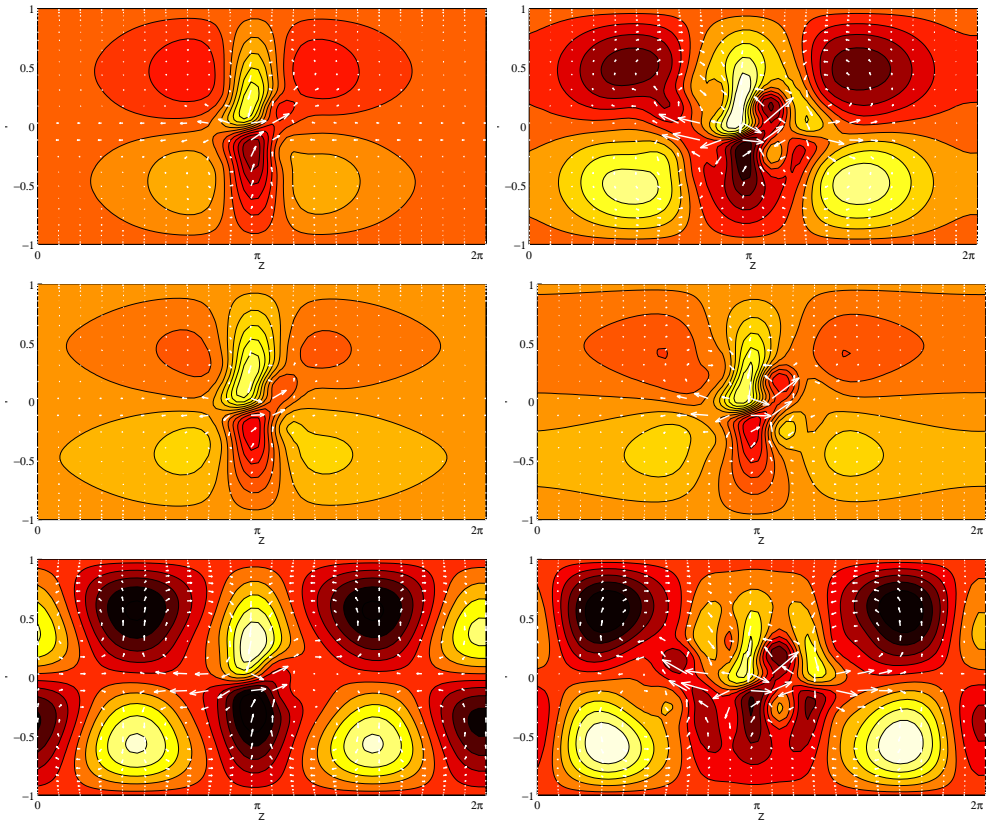

Figure 6: Contours of yz cross-sections of streamwise component of perturbation velocity $\hat{\mathbf{u}}$ (arrows indicate velocity field of $(\hat{\mathbf{v}}, \hat{\mathbf{w}})$ plane) of steady solution EQ7-1 at $Re = 1000$ in box $2\pi \times 2 \times 2\pi$ shown as black circles in figure 4. Top left, pt 7 at $Ri_b = 0$; top right, pt 8 at $Ri_b = 0$; middle left, pt 9 at $Ri_b = 1 \times 10^{-3}$; middle right, pt 10 at $Ri_b = 2.88 \times 10^{-3}$; bottom left pt 11 at $Ri_b = -1.22 \times 10^{-3}$; bottom right, pt 12 at $Ri_b = -9.9 \times 10^{-4}$. All plots have 8 contours between [-0.31, 0.31], which are the minimum and maximum of most energetic state at pt 11 (arrows rescaled as well).

small streamwise rolls are being suppressed by the potential energy penalty imposed by the stable stratification: see §3.4 for further discussion of this.

There is also a difference in continuing EQ7-1 between the two geometries at negative Ri_b where the stratification is unstable: the $4\pi \times 2 \times 2\pi$ EQ7-1 solutions connect to a 2D solution branch of Rayleigh-Benard rolls whereas the $2\pi \times 2 \times 2\pi$ EQ7-1 solutions do not. Figures 6 and 7 indicate how the structure of EQ7-1 varies around these two solutions branches. Figure 7 is particularly interesting as EQ7-1 starts out as spanwise global (top left and point 1 on the 2D convective roll branch in figure 4) and then spanwise localises by point 4 (in figure 4). It achieves this by the flanks of the structure gradually ebbing away as Ri_b is increased which is made clear in figure 8. As discussed in §4.1 of Gibson & Brand (2014), this decay, at least at small amplitudes distant from the core of the flow structure, can be understood by identifying the least *spatially damped* steady eigenfunction of the linear operator based upon the basic state (typically this will be a 2D eigenfunction invariant in the streamwise direction here). One consequence of this is the expectation that the rate of spatial evanescence increases as Ri_b increases away

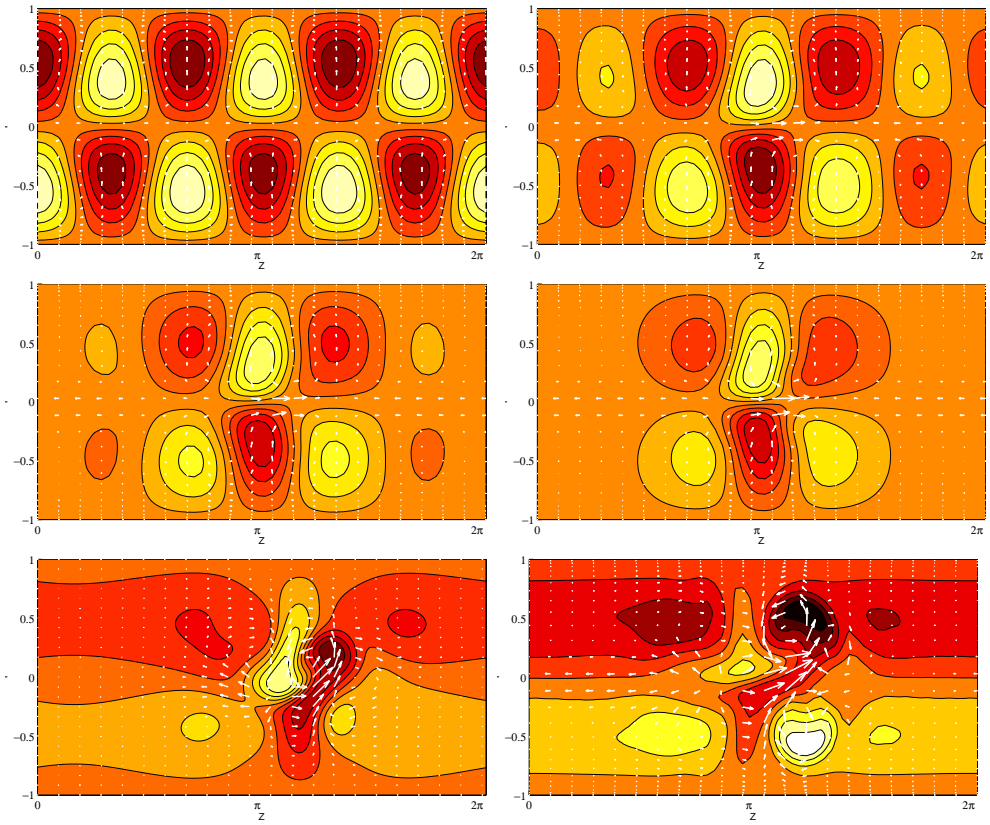

Figure 7: Contours of yz cross-sections of streamwise component of perturbation velocity $\hat{\mathbf{u}}$ (arrows indicate velocity field of $(\hat{\mathbf{v}}, \hat{\mathbf{w}})$ plane) of steady solution EQ7-1 at $Re = 1000$ in box $4\pi \times 2 \times 2\pi$ shown as red triangles in figure 4. Top left pt 1; top right, pt 2; middle left pt 3; middle right, pt 4; bottom left pt 5; bottom right, pt 6. All plots have 8 contours between [-0.48, 0.48], which are the minimum and maximum of state at pt 7 (arrows rescaled as well).

from the bifurcation point where the decay rate is zero. Since the spanwise domain is relatively small, we do not attempt any further analysis here but a similar process is observed when tracking a stratified version of the 'snake' solution of Schneider et al. (2010b) and is analysed in Olvera & Kerswell (2017).

Further edge tracking was done in a domain where the width was halved - so $(Re, Ri_b, L_x, L_z) = (1000, 1 \times 10^{-3}, 2\pi, \pi)$ - which led to a global steady mode: see Figure 9. This solution, which possesses all three symmetries $\mathcal{S}, \Omega$ and $\mathcal{Z}$, is the stratified version of the hairpin vortex solution (HVS) of Itano & Generalis (2009), EQ7 in the nomenclature of Gibson et al. (2009) and the mirror-symmetric solution of Deguchi & Hall (2014, 2015): hereafter we will refer to it as EQ7. The unstratified version has also been found before by edge tracking at the parameter settings $(Re, Ri_b, L_x, L_z) = (1000, 0, 4.35\pi, 1.05\pi)$ (see figure 5 of Rabin et al. (2012)). Figure 4 shows that EQ7 exists significantly *above* the laminar-turbulent boundary: figure 1 indicates that $Ri_b \approx 0.015$ at the boundary for the $2\pi \times 2 \times \pi$ box whereas EQ7 extends up to $Ri_b \approx 0.055$. As observed for EQ7-1, the solution branch for EQ7 turns back to lower Ri_b when the potential energy of the state becomes roughly twice the kinetic energy in the cross-stream (vertical) direction: see

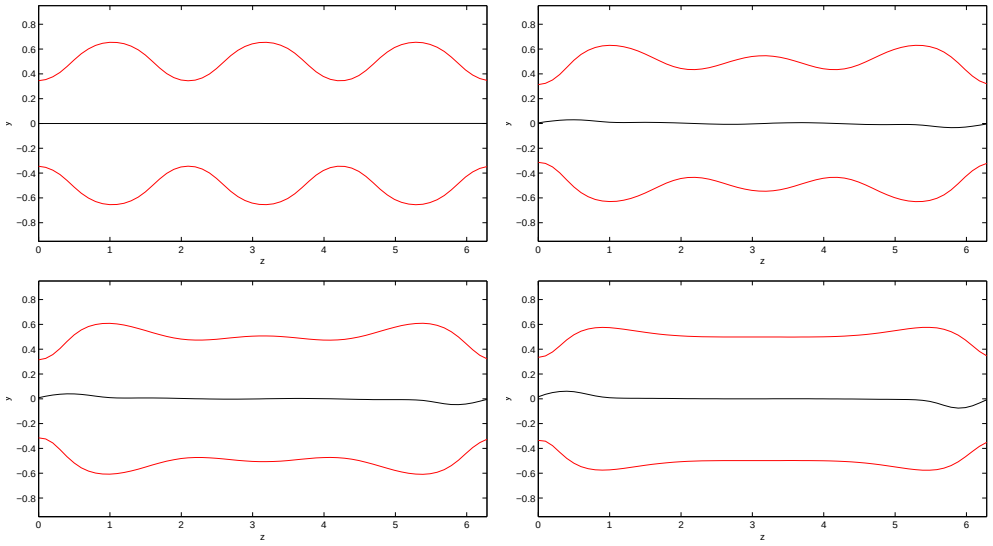

Figure 8: Contours of total velocity $\mathbf{u}$ at levels $\mathbf{u} = \{0, \pm 0.05\}$ of steady solution EQ7-1 at $Re = 1000$ in box $4\pi \times 2 \times 2\pi$ shown as red triangles in figure 4. Top left, pt 1; top right, pt 2; bottom left, pt 3; bottom right, pt 4. All states have been shifted in the spanwise direction by half the domain to highlight the gradual evanescence of the central domain.

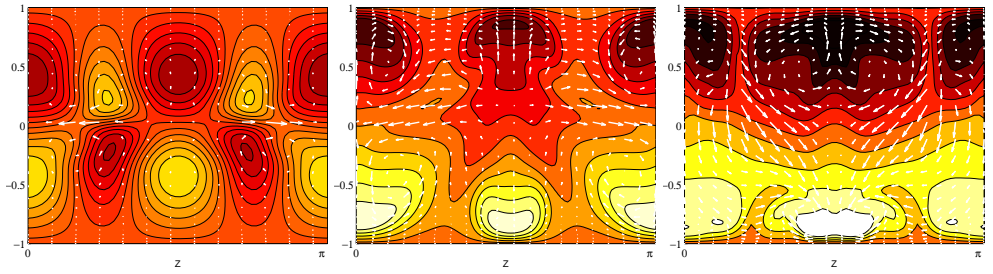

Figure 9: Contours of yz cross-sections of streamwise component of perturbation velocity $\hat{\mathbf{u}}$ (arrows indicate velocity field of $(\hat{\mathbf{v}}, \hat{\mathbf{w}})$ plane) of steady solution EQ7 at $Re = 1000$ in box $2\pi \times 2 \times \pi$ shown as squares in figure 4. Left, pt 13 at $Ri_b = 0.001$; middle, pt 14 at $Ri_b = 0.053$; right, pt 15 at $Ri_b = 0$ upper branch. All plots have 8 contours between[-1.02, 0.83], which are the minimum and maximum of state at pt 13 (arrows rescaled as well).

figure 10. The EQ7 solution branch shown also could not be closed which is investigated in §3.3.

In the hunt for further ECS, edge-tracking was also performed in small domains with various combinations of symmetries imposed and extended (wider or longer) domains (typically with mirror symmetry $\mathcal{Z}$ imposed). However, only chaotic states were found beyond the ECS already identified. For example, edge-tracking in the streamwise-extended domain $(Re, Ri_b, L_x, L_z) = (1000, 1 \times 10^{-3}, 16\pi, 2\pi)$, with and without $\mathcal{Z}$-symmetry imposed, lead to streamwise-localised chaotic states as in Schneider et al. (2010b). Some computations were also done for strong stratification ($Ri_b = 0.1$) and $Re = 10,000$ in

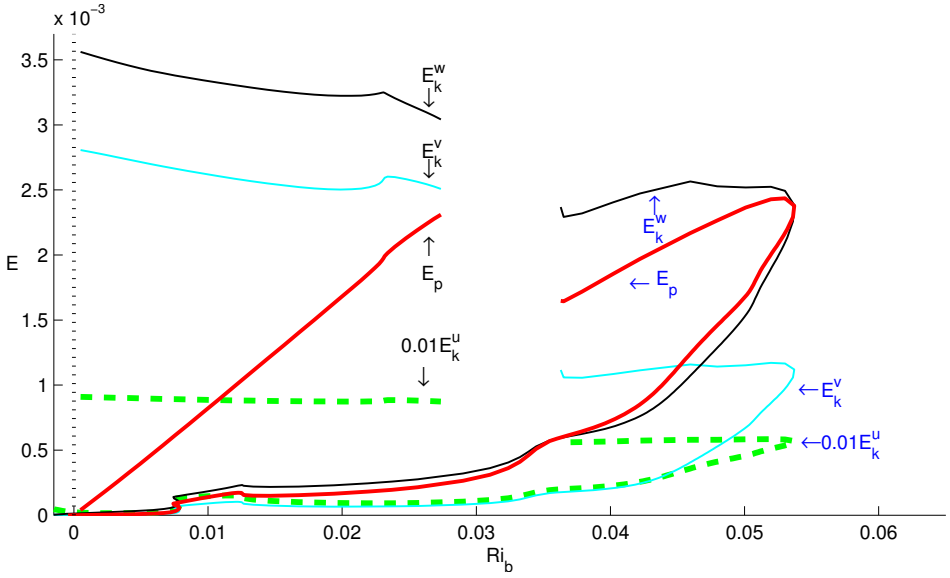

Figure 10: Continuation in Ri_b at $Re = 1000$ for solution EQ7 in box $2\pi \times 2 \times \pi$ (see inset of figure 4). The kinetic energy is splitted into its three components (E_u, E_v and E_w).

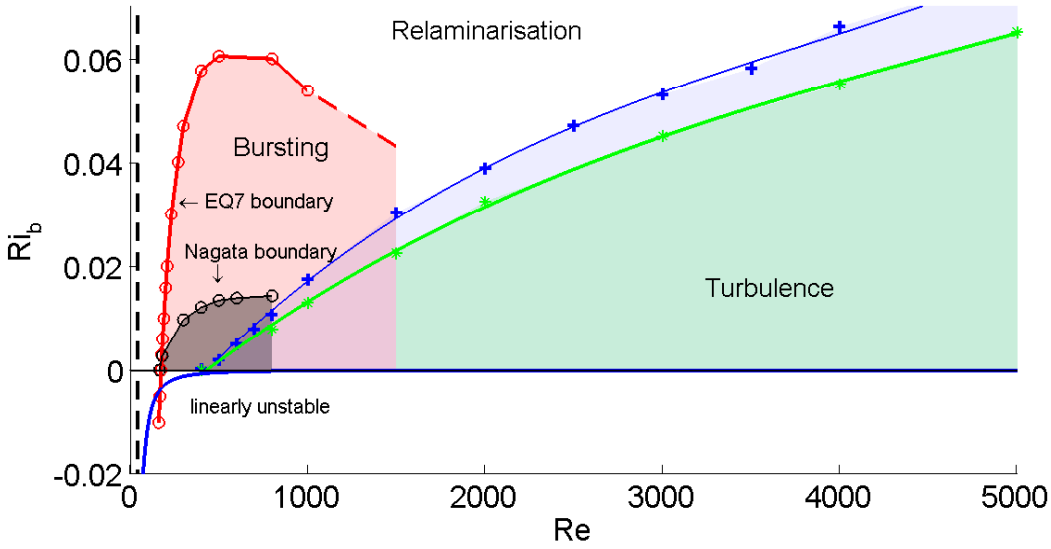

Figure 11: Parameter space (with $Pr = 1$): the (Re, Ri_b) plane. The blue line indicates the turbulent–laminar boundary for box $2\pi \times 2 \times 2\pi$ and the green line for box $2\pi \times 2 \times \pi$. The red line shows the area of existence for EQ7 and its likely continuation is discussed in §3.4.

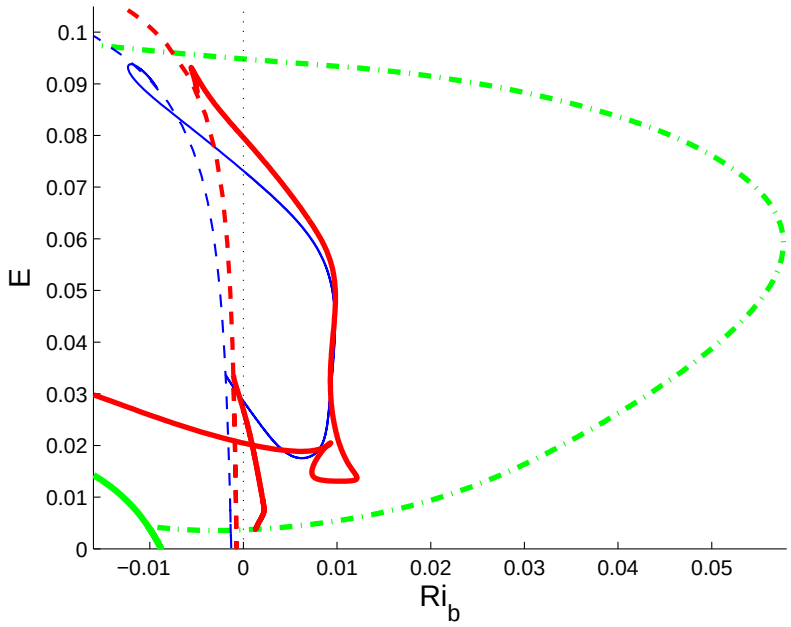

Figure 12: Energy E verses Ri_b for Nagata's solution at $Re = 300$ (thin solid blue line) and $Re = 400$ (thick solid red line) together with EQ7 at $Re = 400$ (green dash-dot line) and 2D convective roll solutions (thin and thick dashed lines and the very thick line in the bottom left corner) for $Ri_b < 0$. The plot shows that Nagatas solution branch is initially (at $Re = 300$) a loop which starts and finishes on a 2D convective roll branch whereas, at $Re = 400$, this loop has broken to connect to the EQ7 solution branch. The upper Nagata solution branch arm then extends back to convectively unstable flows.

small domains but again, only chaotic edge states were found even in really small domains like $\pi \times 2 \times \frac{1}{4}\pi$ constrained by the imposition of the mirror symmetry $\mathcal{Z}$.

Since both EQ7-1 and EQ7 could be continued back to the unstratified limit, $Ri_b = 0$, (see Figure 4) and looked to have all the features associated with SSP/VWI (dominant streaks with secondary streamwise rolls and wave field), no purely-stratified ECS (ECS with no $Ri_b = 0$ limit) were found. Such new ECS probably only exist at much larger Ri_b than that found for $Re = O(5000)$ since the ratio of internal-gravity-wave timescale to advective timescale (h/U) is $1/\sqrt{Ri_b}$. This presumably needs to be $O(1)$ to be important which, as we argue below, only occurs at large Re when the ECS becomes fully localised. The fact that EQ7 exists beyond the laminar-turbulent boundary for the Re examined ($Re \leq 1000$ - see figure 11) at least confirms the general consensus that ECS are a necessary precursor (now as Ri_b *de*creases at fixed Re) for turbulence to be possible. In fact, the region where EQ7 exists but turbulence does not, possesses a 'bursting' phenomenon - see figure 11 - where certain initial conditions can give rise to large energy growth up to energy levels commensurate with the turbulent state at lower Ri_b (see Olvera & Kerswell (2017) for more details). Henceforth we focus on studying EQ7. Before considering the question of how large Ri_b can become and still have ECS, we first examine the stratification of Nagata's (1990) first solution and how it relates to EQ7.

3.3. *EQ7 and Nagata's solution*

Nagata's (1990) solution was the first finite amplitude state discovered in plane Couette flow and it has been known since the work of Clever & Busse (1992) that this solution actually bifurcates off a 2D (single layer) roll solution in Rayleigh-Benard convection (negative Ri_b). It has been found here that EQ7 also bifurcates off a 2D (double layer) roll solution - see figure 12. Since Nagata's solution has one less symmetry than EQ7, one could expect that Nagata's solution bifurcates off EQ7 in a symmetry-breaking bifurcation. This is indeed the case at least at $Re = 400$: see figure 12 which also shows that Ri_b does not need to be increased very far before Nagata's solution ceases to exist compared to EQ7. Figure 11 further emphasizes this.

Before considering EQ7 at large Re, we first return to an issue shown in figure 4. The inset of figure 4 shows two continuations of EQ7 at $Re = 1000$ in a box $2\pi \times 2 \times \pi$, one starting at the edge-tracked solution at $Ri_b = 1 \times 10^{-3}$ (the lower branch) and the other starting from the upper branch solution at $Ri_b = 0$ (obtained by continuing the lower branch solution back to $Ri_b = 0$ and then continuing around the saddle node using the spanwise wavenumber). At lower Re, these two continuations meet (e.g. at $Re = 400$ as shown in figure 12) when varying Ri_b to produce a smooth connection between unstratified upper and lower branch solutions but clearly do not at $Re = 1000$. At $Re = 500$ - see figure 13 - the connection between upper and lower unstratified solutions has broken. Tracing the new crossings of the $Ri_b = 0$ line reveals what looks to be a previously-unknown branch of 'inner' solutions coloured red in figure 14 (left) at $Re = 300$ which bifurcates off a 3D state almost immediately after that bifurcates off a double roll state in Rayleigh-Benard convection ($Ri_b < 0$). A further lower branch break up occurs between $Re = 700$ and $Re = 850$ as shown in figure 14 (right) which finally explains the complicated continuation curve at $Re = 1000$ in the inset to figure 4. Clearly, stable stratification has a strong influence on the states. We now turn our attention to understanding exactly why.

3.4. *EQ7 Asymptotics*

To gain some understanding of how stratification affects the SSP/VWI states at large Re, we concentrate on understanding how the lower branch EQ7 solutions behave as Ri_b is increased from 0 at large Re. Of particular interest is how the maximum Richardson number for such states scales with Re. Figure 16 shows how the wall shear stress deviation Δ varies as Ri_b increases for the lower branch of EQ7. All curves show an initial drop in stress from the unstratified value, a minimum of stress at some finite Ri_b^{min} and then two turning points where the curve reaches a local maximum in $Ri_b := Ri_b^{max}$ and then a local minimum in Ri_b. Four states at $Re = 40,000$ and various values of Ri_b (marked by blue dots in figure 16) are shown in figure 17 which indicates that EQ7 transits from a global flow state to one showing localisation in the cross-shear direction y and further localisation in the spanwise direction z. The first two states, which appear global, can be described as being in regime 1 whereas the second two states, which are clearly localised, indicate a second and possibly third regime.

3.4.1. *Regime 1*

Regime 1 corresponds to the range of Ri_b where a stratified version of the VWI structure of Hall & Sherwin (2010) is realised. The only prior work to consider stratification is Hall (2012) which looked at the natural convection situation where the stratification is parallel to the shear: differences with our case here of stratification *perpendicular* to the shear will be highlighted below. A first key observation is that because EQ7 is steady *and* Ω-symmetric, the critical layer $u = 0$ is always located on $y = 0$ and therefore has

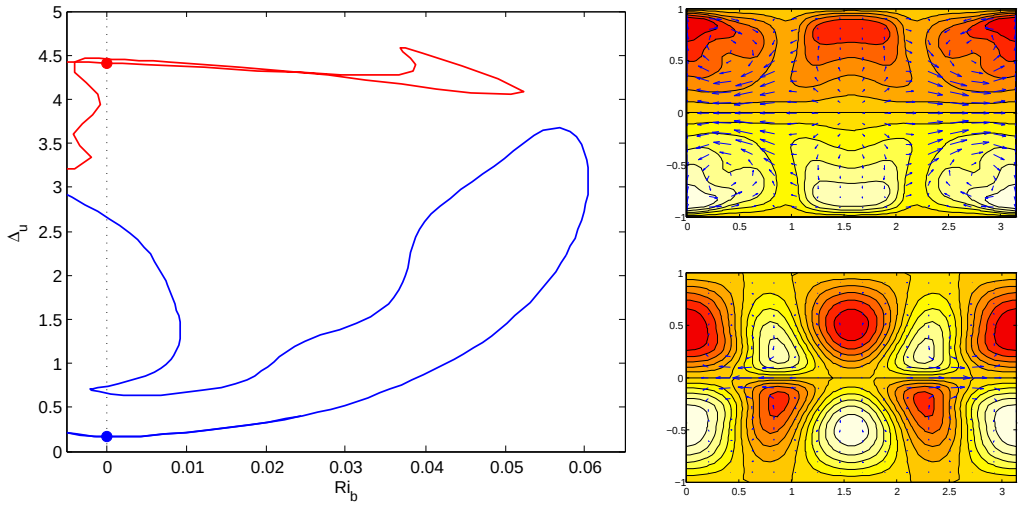

Figure 13: Continuation in Ri_b of EQ7 at $Re = 500$ in a box $2\pi \times 2 \times \pi$. Dots on the $Ri_b = 0$ axis indicate known upper and lower unstratified solutions. The upper right plot shows the state (contours of $\hat{u}$ and arrows for $(\hat{v}, \hat{w})$) at the upper (red) dot (12 contour levels across [-1.02,1.02]) and the lower right plot shows the state at the lower (blue) dot (12 contour levels across [-0.17,0.17]).

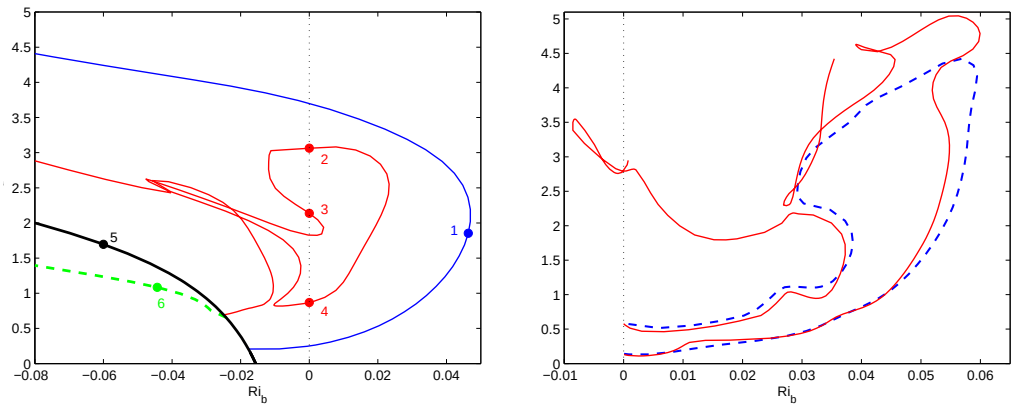

Figure 14: Left: EQ7 continuation in Ri_b at $Re = 300$ in a box $2\pi \times 2 \times \pi$. The inner (red) branch connects to the dashed green 3D branch of x-wavelength π just after it itself bifurcates off the black 2D-roll branch. The outer (blue) branch bifurcates directly off the black 2D-roll branch. Typical resolution used $(M, N, L) = (16, 25, 16)$ and plots of the various states marked by dots and numbers are given in figure 15. Right: Lower branch continuation for EQ7 in Ri_b for at $Re = 700$ (blue dashed line) in a box $2\pi \times 2 \times \pi$ which is comparable with that at $Re = 500$ and $Re = 850$ (red solid line). This plot shows that the lower branch loop at Re=700 has broken up into two disconnected pieces at $Re = 850$ (this break up happens in the interval $(800, 850)$). Typical resolutions used to confirm this behaviour were $(M, N, L) = (12, 25, 16)$, $(14, 40, 20)$ and $(16, 30, 20)$.

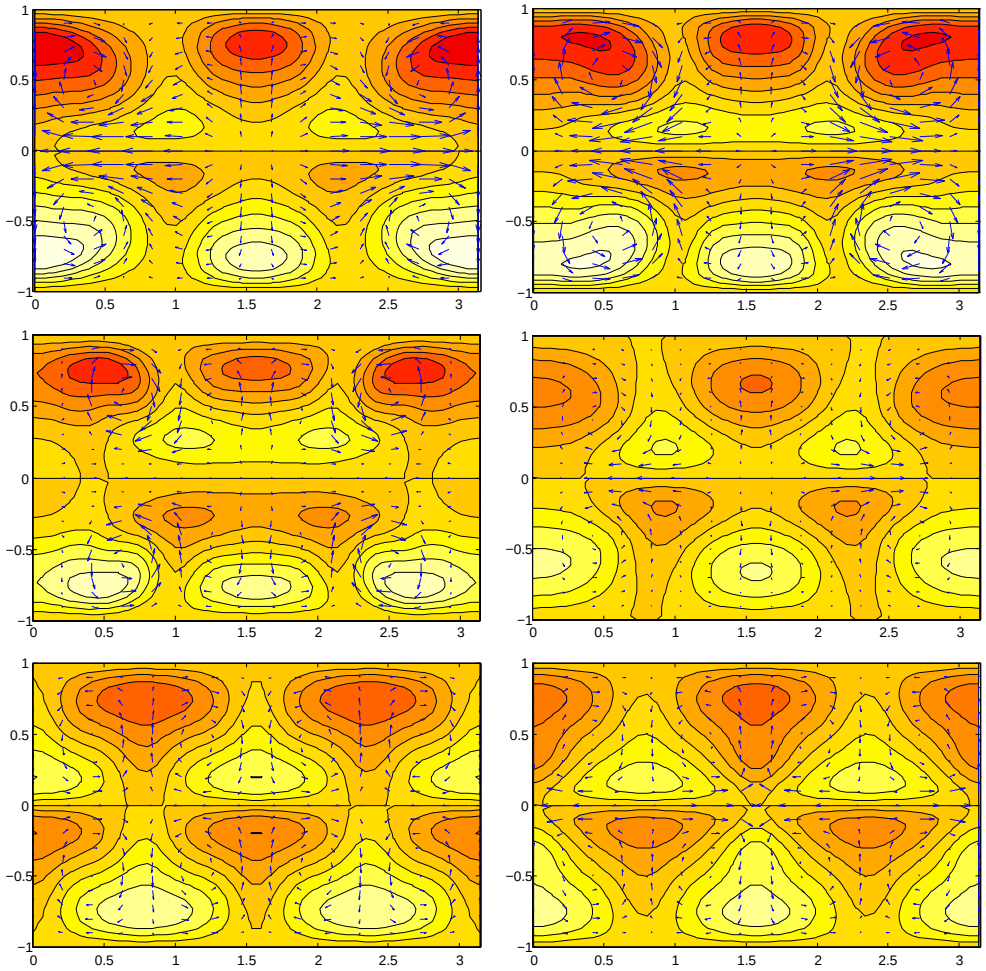

Figure 15: EQ7 flow states (contours of $\hat{u}$ and arrows for $(\hat{v}, \hat{w})$) shown over a y-z plane at $Re = 300$. Upper left state 1 shown in figure 14, upper right state 2, middle left state 3, middle right state 4, lower left state 5 and lower right state 6. There are 12 contours over [-0.725,0.725] (red-white) and max cross-flow speed is 0.296 across *all* plots to show relative strengths of the states.

no curvature. To keep the discussion general, we broaden the direction of gravity $\mathbf{g}$ to $-\cos\theta\hat{\mathbf{y}} - \sin\theta\hat{\mathbf{z}}$ and consider two cases: $\theta = 0$ is 'cross-stream' gravity perpendicular to the boundaries and $\theta = \pi/2$ is 'spanwise' gravity aligned with the boundaries: in the geophysical literature, these limiting cases are usually referred to as 'vertical' and 'horizontal' stratified shear situations respectively. The governing equations in component

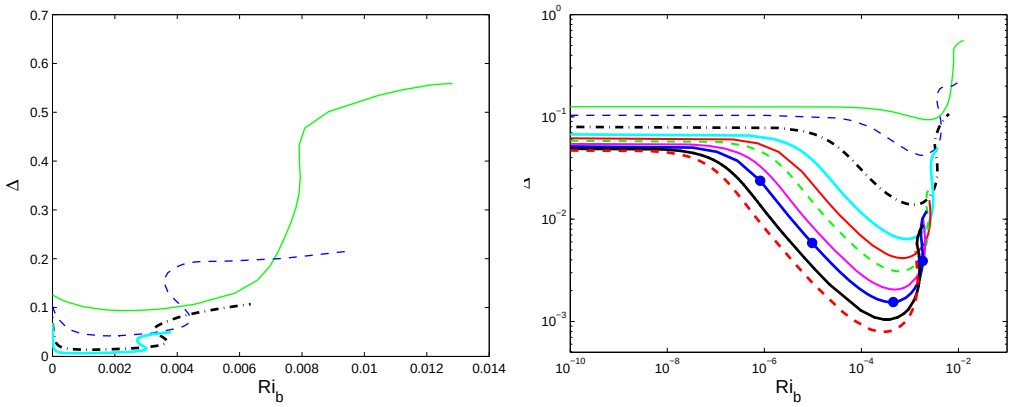

Figure 16: Left. The wall shear stress deviation Δ as a function of Ri_b for the lower branch of EQ7 at $Re = 1000$ (green solid), 2000 (blue dashed), 5000 (black thick dash-dot) and $10,000$ (cyan thick solid). All curves show an initial drop in stress from the unstratified value, a minimum of stress at some finite Ri_b^{min} and two turning points where the curve reaches a local maximum in Ri_b^{max} and then a local minimum in Ri_b. Right. The same data as on the left but plotted on a log-log plot with extra lower branch data (at $15,000$ (red solid), $20,000$ (green dashed), $30,000$ (magenta solid), $40,000$ (blue thick solid, $60,000$ (black thick solid) and $80,000$ (red thick dashed)) added. The velocity states corresponding to the 4 blue dots on the blue $Re = 40,000$ curve - at $Ri_b \approx 10^{-6}, 10^{-5}$, the minium stress point $Ri_b^{min} = 4.15 \times 10^{-4}$ and the local max point $Ri_b^{max} = 1.833 \times 10^{-3}$ - are shown in figure 17.

form for the total fields (recall from (2.7) that $\mathbf{u} = \hat{\mathbf{u}} + y\hat{\mathbf{x}}$ and $\rho = \hat{\rho} - y$) are

$$u_t + uu_x + vu_y + wu_z + p_x = \frac{1}{Re}\nabla^2 u, \tag{3.1}$$

$$v_t + uv_x + vv_y + wv_z + p_y = \frac{1}{Re}\nabla^2 v - Ri_b\ \rho\cos\theta, \tag{3.2}$$

$$w_t + uw_x + vw_y + ww_z + p_z = \frac{1}{Re}\nabla^2 w - Ri_b\ \rho\sin\theta, \tag{3.3}$$

$$\rho_t + u\rho_x + v\rho_y + w\rho_z = \frac{1}{RePr}\nabla^2 \rho, \tag{3.4}$$

$$u_x + v_y + w_z = 0. \tag{3.5}$$

Note also that the effect of the transformations $\mathcal{S}, \Omega$ and $\mathcal{Z}$ detailed in (2.8), (2.9) and (2.10) is for the (original) $\theta = 0$ case where the transformations experienced by v and ρ match: for $\theta = \pi/2$ the transformation properties of ρ have to be changed to match those of w and for general θ there are no such symmetries). Following Hall & Sherwin

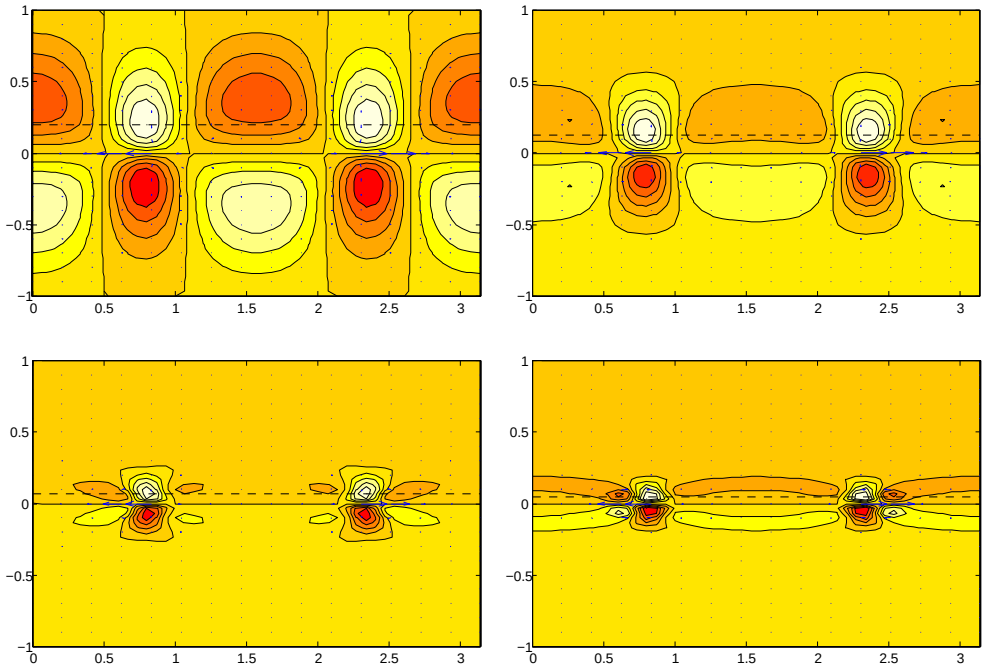

Figure 17: EQ7 flow states (contours of $\hat{u}$ and arrows for $(\hat{v}, \hat{w})$) shown over a y-z plane at $Re = 40,000$. The states correspond to the blue dots in figure 16 (right) with the order upper left, upper right, lower left (the stress minimum), lower right corresponding to increasing Ri_b . The contour levels for the streamwise velocity perturbation $\hat{u} = u - y$ (the arrows indicate $v\hat{\mathbf{y}} + w\hat{\mathbf{z}}$) are as follows: upper left, 10 contours between $\pm 6.73 \times 10^{-2}$ (arrow max 1.0×10^{-3}); upper right, 10 contours between $\pm 3.8 \times 10^{-2}$ (arrow max 1.1×10^{-3}) ; lower left, 10 contours between $\pm 1.81 \times 10^{-2}$ (arrow max 1.8×10^{-3}); and lower right, 10 contours between $\pm 2.31 \times 10^{-2}$ (arrow max 2.51×10^{-3}). The dashed black lines on each plot correspond to the y level of the corresponding $x - z$ slices shown in figure 18.

(2010), we look for steady solutions *away* from the critical layer of the form

$$\begin{aligned}
u &= \bar{u}(y,z) + \ldots &&+ \delta Re^{-1/3}(U(y,z)e^{i\alpha x} + c.c) + \ldots,\\
v &= Re^{-1}\bar{v}(y,z) + \ldots &&+ \delta Re^{-1/3}(V(y,z)e^{i\alpha x} + c.c) + \ldots,\\
w &= Re^{-1}\bar{w}(y,z) + \ldots &&+ \delta Re^{-1/3}(W(y,z)e^{i\alpha x} + c.c) + \ldots,\\
\rho &= \bar{\rho}(y,z) + \ldots &&+ \delta Re^{-1/3}(R(y,z)e^{i\alpha x} + c.c) + \ldots,\\
p &= Re^{-2}\bar{p}(y,z) + \ldots &&+ \delta Re^{-1/3}(P(y,z)e^{i\alpha x} + c.c) + \ldots
\end{aligned}$$

where *c.c.* denotes complex conjugate and all components of the wave field (U, V, W, R, P) are assumed of equal magnitude consistent with spatial scales being similar in every direction. The small parameter $Re^{-1/3}$ is the usual scaling for a critical layer where advection by the mean flow is balanced by viscous terms (e.g. see Hall & Sherwin (2010)), and δ is the wave amplitude *in* the critical layer to be determined later. Substituting these expansions into equations (3.1)-(3.4) gives, to leading order in Re, for the x-independent

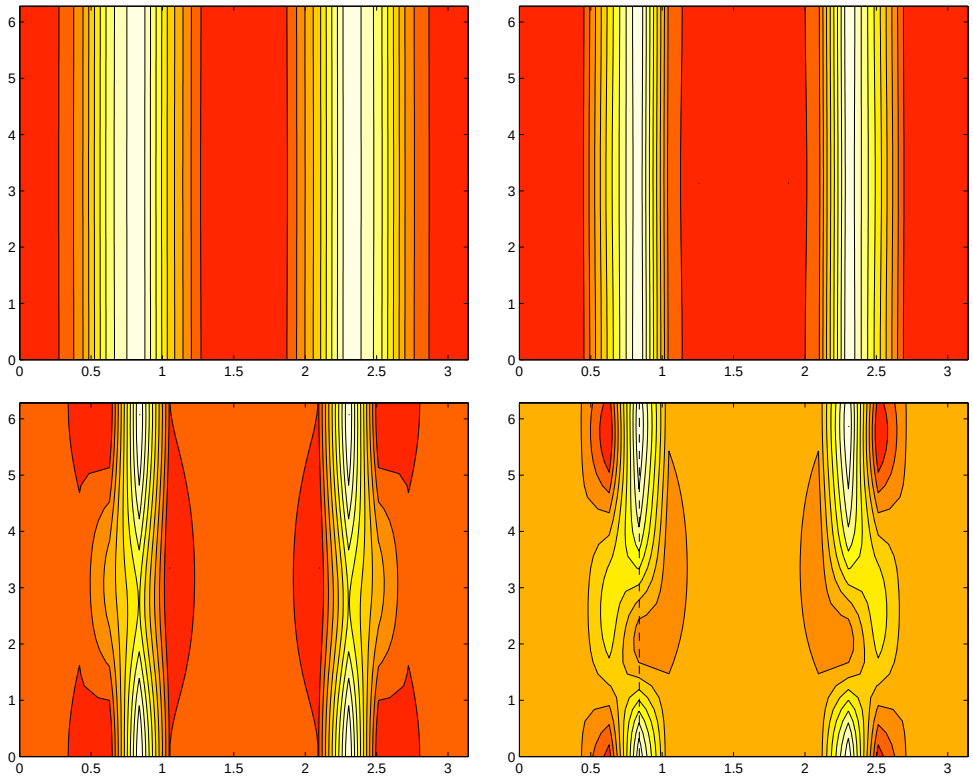

Figure 18: EQ7 flow states shown over a x-z plane at $Re = 40,000$ and the y levels shown in figure 17 ($y = 0.2$, 0.13, 0.07 and 0.05 respectively). The contour levels for the streamwise velocity perturbation $u - y$ are as follows: upper left, 10 contours across $[-0.042, 0.061]$; upper right, 10 contours across $[-0.0142, 0.033]$; lower left, 10 contours across $[-0.00669, 0.0166]$; and lower right, 10 contours across $[-0.0216, 0.0239]$.

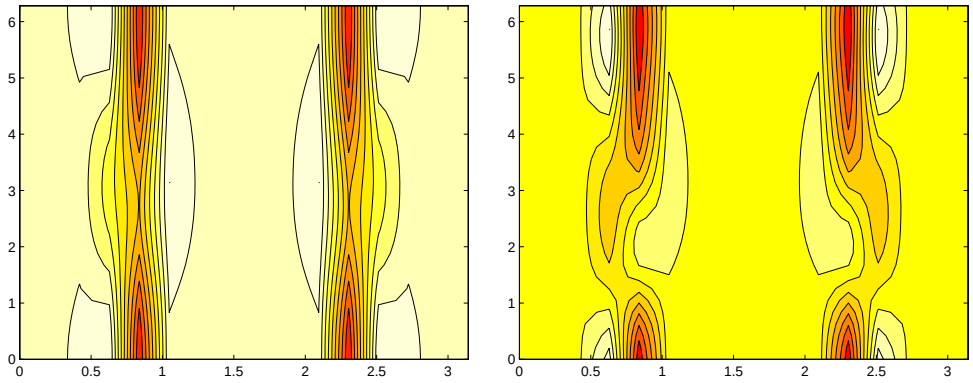

Figure 19: The density perturbation $\rho + y$ for the 3rd and 4th EQ7 flow states shown in figures 17 and 18 over a x-z plane at $y = 0.07$ (left) and 0.05 (right). The contour levels are as follows: left, 10 contours across $[-0.0167, 0.00692]$; and right, 10 contours across $[-0.024, 0.022]$.

part (the roll and streak equations)

$$\bar{v}\bar{u}_y + \bar{w}\bar{u}_z = \bar{u}_{yy} + \bar{u}_{zz}, \tag{3.6}$$

$$\bar{v}\bar{v}_y + \bar{w}\bar{v}_z + \bar{p}_y = \bar{v}_{yy} + \bar{v}_{zz} - Re^2 Ri_b\ \bar{\rho}\cos\theta, \tag{3.7}$$

$$\bar{v}\bar{w}_y + \bar{w}\bar{w}_z + \bar{p}_z = \bar{w}_{yy} + \bar{w}_{zz} - Re^2 Ri_b\ \bar{\rho}\sin\theta, \tag{3.8}$$

$$\bar{v}\bar{\rho}_y + \bar{w}\bar{\rho}_z = \frac{1}{Pr}(\bar{\rho}_{yy} + \bar{\rho}_{zz}), \tag{3.9}$$

$$\bar{v}_y + \bar{w}_z = 0 \tag{3.10}$$

and for the x-dependent (wave) part

$$i\alpha\bar{u}U + V\bar{u}_y + W\bar{u}_z + i\alpha P = 0, \tag{3.11}$$

$$i\alpha\bar{u}V + P_y = -Ri_b\ R\cos\theta, \tag{3.12}$$

$$i\alpha\bar{u}W + P_z = -Ri_b\ R\sin\theta, \tag{3.13}$$

$$i\alpha\bar{u}R + V\bar{\rho}_y + W\bar{\rho}_z = 0, \tag{3.14}$$

$$i\alpha U + V_y + W_z = 0 \tag{3.15}$$

which is just the inviscid linearised Navier-Stokes about the streak field with critical layer at $\bar{u}(y,z) = 0$. In the x-independent equations (3.6)-(3.10), the leading nonlinear terms due to the wave field are $O(\delta^2 Re^{1/3})$ smaller in the $\bar{u}$ and $\bar{\rho}$ equations and $O(\delta^2 Re^{4/3})$ smaller in the $\bar{v}$ and $\bar{w}$ equations. Therefore, providing $\delta = o(Re^{-2/3})$, the rolls and streaks are unforced in the interior and so, if they are not to slowly dissipate, must be forced by the critical layer through matching conditions across it - this is the essence of the Vortex-Wave-Interaction theory of (Hall & Sherwin 2010). Also at this point it is clear that stratification first affects the roll equations when $Ri_b \sim 1/Re^2$ as opposed to $Ri_b \sim 1/Re$ for stratification (gravity) aligned with the shear direction (Hall 2012) where the right hand side of (3.6) would be $\bar{u}_{yy} + \bar{u}_{zz} - ReRi_b\bar{\rho}$). This, of course, is because the (streamwise) rolls are $O(1/Re)$ smaller than the streaks and therefore more easily affected.

In the critical layer around $\bar{u}(y,z) = 0$ (here, conveniently, just the plane $y = 0$), assuming $\bar{p}$ does not vanish at the critical layer $y = 0$ and $\bar{u}(y,z)$ has a simple zero at $y = 0$, equations (3.11)-(3.14) indicate that $U, V, W \sim 1/y$ and $R \sim 1/y^2$ as $y \to 0$. Since $y = O(Re^{-1/3})$ in the critical layer, the U and W fields are $O(Re^{1/3})$ larger in the critical layer than outside and R is $O(Re^{2/3})$ larger. The V field cannot be similarly $O(Re^{1/3})$ larger due to incompressibility so remains $O(\delta Re^{-1/3})$ and therefore matches to a higher order outer component on the outside. This thinking motivates the expansions *inside* the critical layer of

$$\begin{aligned}
u &= Re^{-1/3}Y\frac{d\bar{u}}{dy}(0,z) + \delta^2 Re^{1/3}\bar{u}^c(Y,z) + \ldots + \delta(\mathcal{U}(Y,z)e^{i\alpha x} + c.c) + \ldots,\\
v &= Re^{-4/3}Y\frac{d\bar{v}}{dy}(0,z) + \delta^2\bar{v}^c(Y,z) + \ldots \qquad + \delta Re^{-1/3}(\mathcal{V}(Y,z)e^{i\alpha x} + c.c) + \ldots,\\
w &= Re^{-1}\bar{w}(0,z) \qquad + \delta^2 Re^{1/3}\bar{w}^c(Y,z) + \ldots + \delta(\mathcal{W}(Y,z)e^{i\alpha x} + c.c) + \ldots,\\
\rho &= \qquad \bar{\rho}(0,z) \qquad + \delta^2 Re^{2/3}\bar{\rho}^c(Y,z) + \ldots \quad + \delta Re^{1/3}(\mathcal{R}(Y,z)e^{i\alpha x} + c.c) + \ldots,\\
p &= Re^{-2}\bar{p}(0,z) \qquad + \delta^2 Re^{-2/3}\bar{p}^c(Y,z) + \ldots + \delta Re^{-1/3}(\mathcal{P}(Y,z)e^{i\alpha x} + c.c) + \ldots
\end{aligned}$$

where $Y := Re^{1/3}y$. For $\theta = 0$, $\bar{u}(0,z) = \bar{v}(0,z) = \bar{\rho}(0,z) = 0$ (by the Ω symmetry) whereas for $\theta = \pi/2$ $\bar{\rho}(0,z)$ is not zero, so the expansions for u and v reflect this while

that for ρ is kept general. The critical layer wave equations are to leading order

$$i\alpha Y\frac{d\bar{u}}{dy}(0,z)\mathcal{U}+\mathcal{V}\frac{d\bar{u}}{dy}(0,z)+\mathcal{W}Y\frac{d^2\bar{u}}{dydz}(0,z)+i\alpha\mathcal{P}=\mathcal{U}_{YY}, \tag{3.16}$$

$$i\alpha Y\frac{d\bar{u}}{dy}(0,z)\,\mathcal{V} \qquad +Re^{2/3}\mathcal{P}_Y=\mathcal{V}_{YY}-ReRi_b\,\mathcal{R}\cos\theta, \tag{3.17}$$

$$i\alpha Y\frac{d\bar{u}}{dy}(0,z)\,\mathcal{W} \qquad +\mathcal{P}_z=\mathcal{W}_{YY}-Re^{2/3}Ri_b\,\mathcal{R}\sin\theta, \tag{3.18}$$

$$i\alpha Y\frac{d\bar{u}}{dy}(0,z)\,\mathcal{R}+\mathcal{W}\bar{\rho}(0,z)_z \qquad =1/Pr\,\mathcal{R}_{YY}, \tag{3.19}$$

$$i\alpha\mathcal{U}+\mathcal{V}_Y+\mathcal{W}_z=0 \tag{3.20}$$

assuming $\delta=o(Re^{-1/3})$ so that there is no nonlinear feedback. The scalings for the x-independent critical layer variables (indicated with an overbar and superscript ^{c}) follow by ensuring that the leading nonlinear interaction of the wave is balanced in the various components of the equations. Specifically, the dominant balances are

$$(i\alpha\mathcal{U}^*\mathcal{U}+\mathcal{V}^*\mathcal{U}_Y+\mathcal{W}^*\mathcal{U}_Z+c.c.) \;=\; \bar{u}^c_{YY}, \tag{3.21}$$

$$(i\alpha\mathcal{U}^*\mathcal{V}+\mathcal{V}^*\mathcal{V}_Y+\mathcal{W}^*\mathcal{V}_Z+c.c.)+\bar{p}^c_Y \;=\; \bar{v}^c_{YY}-\quad ReRi_b\,\bar{\rho}^c\cos\theta, \tag{3.22}$$

$$(i\alpha\mathcal{U}^*\mathcal{W}+\mathcal{V}^*\mathcal{W}_Y+\mathcal{W}^*\mathcal{W}_Z+c.c.) \;=\; \bar{w}^c_{YY}-Re^{2/3}Ri_b\,\bar{\rho}^c\sin\theta, \tag{3.23}$$

$$(i\alpha\mathcal{U}^*\mathcal{R}+\mathcal{V}^*\mathcal{R}_Y+\mathcal{W}^*\mathcal{R}_z+c.c.) \;=\; \frac{1}{Pr}\,\bar{\rho}^c_{YY}, \tag{3.24}$$

$$\bar{v}^c_Y+\bar{w}^c_Z \;=\; 0. \tag{3.25}$$

Beyond the addition of stratification, the difference here from the analysis of Hall & Sherwin (2010) is the lack of critical layer curvature. The presence of such curvature means that a pressure correction $\bar{p}^c$ must exist of $O(\delta^2Re^{-1/3})$ (so $\bar{p}^c_y=O(\delta^2)$) to supply the necessary centripetal force to produce the curvature of the spanwise flow component along the critical layer (see equation (2.22) of Hall & Sherwin (2010)). With no curvature, the pressure correction is $O(Re^{1/3})$ smaller so there is no longer a pressure jump across the critical layer and the dominant balance is more complicated (see (3.22)). This difference, however, has no effect on the key momentum balance *along* the critical layer which sets the size of δ. Here, regardless of whether $\bar{p}^c$ is $O(\delta^2Re^{-1/3})$ or $O(\delta^2Re^{-2/3})$ as here, this pressure is subdominant to the other terms shown in (3.23) which is equivalent to equation (2.21) in Hall & Sherwin (2010). Now the key realisation is that there must be some jump across the critical layer to energise the rolls otherwise they would decay. This jump occurs first for the tangential rather than normal flow component as δ increases from 0 and can take a number of forms. The jump could be in the tangential velocity component $\bar{w}$ itself which would require $\bar{w}^c=O(Re^{-1})$ or in the 1st normal derivative $\partial\bar{w}^c/\partial y$ which would require $\bar{w}^c=O(Re^{-4/3})$ or even in the 2nd normal derivative $\partial^2\bar{w}^c/\partial y^2$ which would require $\bar{w}^c=O(Re^{-5/3})$. The corresponding scalings for δ would be $Re^{-2/3}$, $Re^{-5/6}$ and Re^{-1} respectively with the middle scaling discussed by Hall & Sherwin (2010) as VWI (presumably a jump in the 2nd derivative is too weak to offset the secular damping of the rolls). There is no jump in the density across the critical layer as $\bar{\rho}^c$ is an $O(Re^{-1})$ smaller than the outer field which is also the situation in the natural convection situation (stratification parallel to the plate flow direction) (Hall 2012).

It is now possible to see that the VWI process first feels the presence of either horizontal or vertical stratification when $Ri_b=O(Re^{-2})$ in the roll equations (3.7)-(3.8) of the interior away from the critical layer. In the critical layer, stratification needs to be

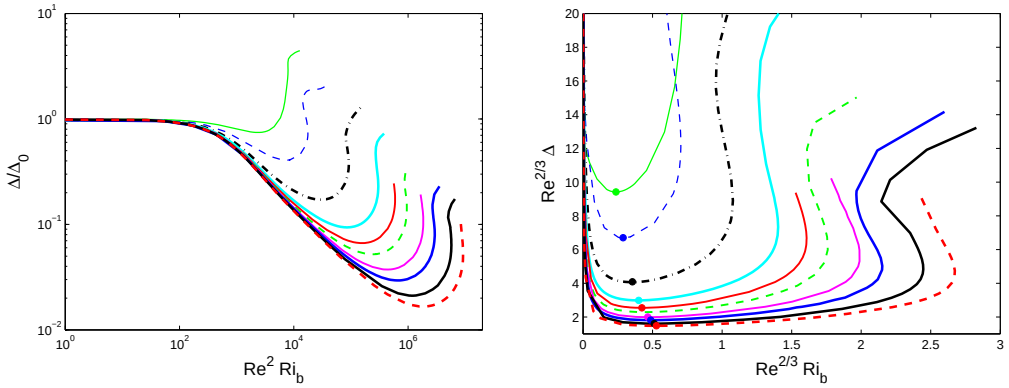

Figure 20: Left. Regime 1: wall shear stress deviation normalised by Δ_0 (its value at $Ri_b = 0$) verses $Re^2 Ri_b$. Right. Regime 2: compensated wall stress $Re^{2/3}\Delta$ verses $Re^{2/3} Ri_b$ (colours as in figure 16). The dot on each curve marks the position of Ri_b^{min} while Ri_b^{max} corresponds to the rightmost turning point on each curve.

much stronger to affect matters, specifically $Ri_b = O(Re^{-1})$ for vertical stratification - see (3.17) and (3.22) - and $Ri_b = O(Re^{-2/3})$ for horizontal stratification - see (3.18) and (3.23). Physically, stratification inhibits motions directed against gravity imposing a potential energy penalty. For both horizontal and vertical stratification, the most immediate impact of this is on the weak $O(Re^{-1})$ rolls and the scaling $Ri_b = O(Re^{-2})$ is precisely when their kinetic energy becomes comparable to the potential energy which is $O(Ri_b)$. Figure 20 (left) confirms this scaling as Ri_b increases from zero which is just a statement that the Rayleigh number, $Ra := -Ri_b Re^2 Pr$, is $O(1)$. This scaling was proposed by Eaves & Caulfield (2015) by heuristic arguments and has also been independently found recently by Deguchi (2017).

3.4.2. *Regime 2*

When $Ri_b \gg O(Re^{-2})$ regime 1 must give way to another regime. Figures 17 and 18 indicate that $\hat{\mathbf{u}}$ and $\hat{\rho}$ localize in the spanwise and cross-stream directions yet stay global in the streamwise direction. This adjustment can be captured by the rescaling

$$(\partial_y, \partial_z) \to (\partial_y, \partial_z)/\epsilon \quad \text{and} \quad (\bar{u}, \bar{v}, \bar{w}, \bar{\rho}) \to (\epsilon\bar{u}, \bar{v}/\epsilon, \bar{w}/\epsilon, \epsilon\bar{\rho}) \tag{3.26}$$

where $\epsilon := (Re^2 Ri_b)^{-1/4} \ll 1$ for $Ri_b \gg Re^{-2}$ indicates the scale of localisation in both cross-stream and spanwise directions. This preserves the form of the equations for the roll, streak and streamwise-averaged density fields yet accommodates the enlarged buoyancy term in the roll equations (either (3.7) or (3.8)). The rescaling for $\bar{u}$ and $\bar{\rho}$ comes from the fact that the streaks and $\bar{\rho}$ only now extend over a cross-stream distance of $O(\epsilon)$ of the underlying applied shear and density fields. A similar scaling was discussed in Blackburn et al. (2013) for unstratified flows when considering the large spanwise wavenumber limit of the SSP/VWI process. Here, the rescaling is driven by increasing Ri_b but the overall effect is the same except there is no localisation in the streamwise direction. This rescaling accommodates increasing stratification until the spanwise localisation of the streamwise-independent fields approaches the critical layer scaling of $Re^{-1/3}$ i.e. when

$$\epsilon = O(Re^{-1/3}) \quad \to \quad Ri_b = O(Re^{-2/3}). \tag{3.27}$$

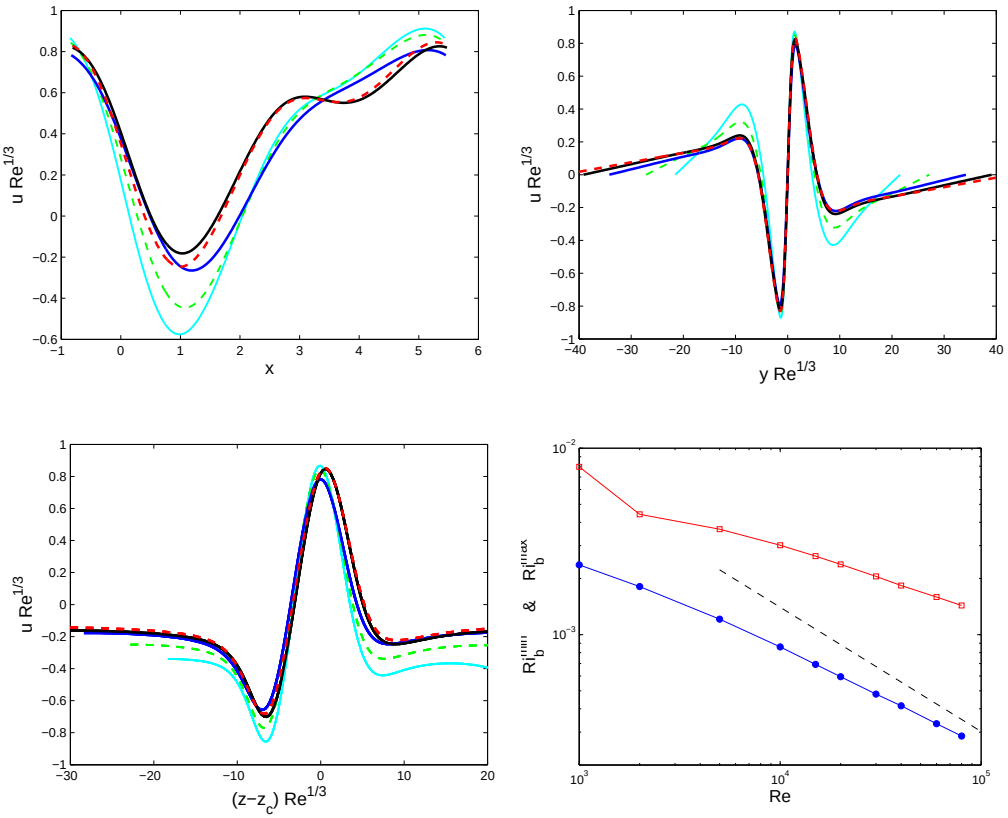

Figure 21: Selected profiles through the streamwise velocity perturbation at Ri_b^{max} for $Re/10,000 = 1$, 2, 4, 6 and 8. Upper left. $Re^{1/3}u(x, y_c(Re/10000), z_c)$ verses x where $y_c(1) = 0.0675$, $y_c(2) = 0.0575$, $y_c(4) = 0.05$, $y_c(6) = 0.04$ and $y_c(8) = 0.035$ are the approximate levels of the streak core shown, for example, in figure 17 (lower right) for $Re = 40,000$. Upper right. $Re^{1/3}u(0, y, z_c)$ verses $Re^{1/3}y$ where $z_c \approx 0.83$ is the spanwise position of the (left) streak core. Lower left. $Re^{1/3}u(0, y_c(Re), z)$ verses $Re^{1/3}(z - z_c)$ (colours as in figure 16). Lower right. $Ri_b^{min}(Re)$ (blue line with dots) where Δ reaches a minimum as Ri_b increases from zero and $Ri_b^{max}(Re)$ (red line with open squares) where the $\Delta - Ri_b$ curve turns around verses Re. The dashed black guideline indicates a scaling of $Re^{-2/3}$.

At this point, the whole perturbation velocity and density fields are confined to the critical 'layer' which is actually a region localised in both cross-stream and spanwise directions. In this, viscosity is important and the rolls and waves are indistinquishable requiring a new asymptotic description. The Boundary Reduced Equations (BREs) of Deguchi, Hall & Walton (2013) and Deguchi & Hall (2015) then seem the only viable rescaling to reflect this new structure. In these, a new spanwise variable $Z := Re^{1/3}(z - z_c)$ (where z_c is the centre of the localised structure) is defined along with the cross-shear critical layer variable $Y := Re^{1/3}y$ in regime 1. Concentrating on the vertical stratification situation

and essentially following Deguchi & Hall (2015), we write

$$u = Re^{-1/3}[\,Y + U(x,Y,Z)\,] + Re^{-2/3}U_1(x,Y) + Re^{-1}d_uY + \dots \tag{3.28}$$

$$v = Re^{-2/3}V(x,Y,Z) + Re^{-1}V_1(x,Y) + \dots \tag{3.29}$$

$$w = Re^{-2/3}W(x,Y,Z) + \dots \tag{3.30}$$

$$p = Re^{-4/3}[\,\frac{1}{2}Ri_bRe^{2/3}Y^2 + P(x,Y,Z)\,] + Re^{-5/3}P_1(x,Y) + \dots \tag{3.31}$$

$$\rho = Re^{-1/3}[\,-Y + R(x,Y,Z)\,] + Re^{-2/3}R_1(x,Y) + Re^{-1}d_\rho Y + \dots \tag{3.32}$$

The rationale behind this expansion is the realisation that the leading fields (U,V,W,P,R) are concentrated over a reduced scale $O(Re^{-1/3})$ in z so spanwise-averaging produces fields $O(Re^{1/3})$ smaller, that is

$$\langle u\rangle = \quad y + Re^{-2/3}[\,U_1(x,Y) + d_uy\,] + \dots, \tag{3.33}$$

$$\langle v\rangle = \quad Re^{-1}V_1(x,Y) + \dots, \tag{3.34}$$

$$\langle w\rangle = \quad 0 \qquad \text{(by symmetry)}, \tag{3.35}$$

$$\langle p\rangle = \quad \frac{1}{2}Ri_by^2 + Re^{-5/3}P_1(x,Y) + \dots, \tag{3.36}$$

$$\langle \rho\rangle = \quad -y + Re^{-2/3}[\,R_1(x,Y) + d_\rho y\,] + \dots, \tag{3.37}$$

since $y = Re^{-1/3}Y$ and

$$\langle\,(U,V,W,P,R)\,\rangle = (0,0,0,0,0) \qquad \text{where } \langle(\quad)\rangle := \frac{1}{L_z}\int_0^{L_z}(\quad)\,dz. \tag{3.38}$$

These scalings give the leading balance

$$(Y+U)U_x + V(1+U_Y) + WU_Z = U_{YY} + U_{ZZ}, \tag{3.39}$$

$$(Y+U)V_x + VV_Y + WV_Z + P_Y = V_{YY} + V_{ZZ} - Ri_bRe^{2/3}R, \tag{3.40}$$

$$(Y+U)W_x + VW_Y + WW_Z + P_Z = W_{YY} + W_{ZZ}, \tag{3.41}$$

$$U_x + V_Y + W_Z = 0, \tag{3.42}$$

$$UR_x + V(-1+R_Y) + WR_Z = \frac{1}{Pr}(R_{YY} + R_{ZZ}) \tag{3.43}$$

to be solved with periodic boundary conditions in x and asymptotically decaying boundary conditions that $(U,V,W,R) \to (0,0,0,0)$ as $Y \,\&\, Z \to \pm\infty$ since no other possibility with vanishing spanwise average can connect to linear profiles in an unforced exterior. The spanwise-averaged problem is

$$\langle\,(U^2)_x + (UV)_Y\,\rangle = U_{1,YY}, \tag{3.44}$$

$$\langle\,(UV)_x + (V^2)_Y\,\rangle = V_{1,YY} - P_{1,Y} - Ri_bRe^{2/3}R_1, \tag{3.45}$$

$$0 = U_{1,x} + V_{1,Y}, \tag{3.46}$$

$$\langle\,(UR)_x + (VR)_Y\,\rangle = \frac{1}{Pr}R_{1,YY}. \tag{3.47}$$

The problem (3.44)-(3.47) is then really just one in U_1 and R_1 which are each computed by two quadratures of (3.44) and (3.47) respectively (V_1 is then found by one quadrature of $-U_{1,x}$ and P_1 follows from (3.45)). In fact, all the computed solutions indicate that $U = -R$ (recall $Pr = 1$) - for example see figure 19 - and hence $U_1 = -R_1$. The spanwise-averaged problem then boils down to solving (3.44) which requires $\langle(U^2)_x\rangle$ integrated twice and $\langle(UV)\rangle$ integrated once with respect to Y. Assuming that U and

V vanish fast enough as $Y \to \pm\infty$, the first term can be expected to drive a particular solution for U_1 odd in Y (as $\langle (U^2)_x \rangle$ is odd in Y) with limiting behaviour $A(x)Y$ for some function $A(x)$. This behaviour must be eliminated by the complementary solution otherwise a mean flow correction of $O(Re^{1/3})$ arises in the exterior inconsistent with (3.38). Integrating $\langle (UV) \rangle$ once can be expected to drive a particular solution for U_1 which asymptotes to one function $B(x) - d_u(x)$ for $Y \to \infty$ and another $B(x) + d_u(x)$ for $Y \to -\infty$ as $\langle (UV) \rangle$ has no particular symmetry in Y. Given the need to match onto simple shears and density gradients in the exterior dependent only on y and the antisymmetry of the mean flow and density gradient, B and d_u must be simple constants and a further contribution from the complementary solution of the form $-B$ needs to be invoked to antisymmetrise the limiting asymptotic behaviour. Hence, a solution for U_1 should be sought with $(U_1, V_1, W_1, R_1) \to (\mp d_u, 0, 0, \pm d_\rho)$ as $Y \to \pm\infty$ (with $d_\rho = -d_u$ inferred by observation). These boundary conditions together with the expansions in (3.28) and (3.32) ensure that the exterior solution just represents a shifted shear in u and gradient in ρ consistent with the imposed conditions on $y = \pm 1$ (see Deguchi & Hall (2014, 2015)). The upshot of all this is a prediction for the mean shear deviation Δ of $d_u Re^{-2/3}$ as in Deguchi & Hall (2015) in this second regime - regime 2 - which is reached when $Ri_b = O(Re^{-2/3})$ (see (3.40) and (3.45)). In the unstratified situation, the BRE regime is only reached when the streamwise wavenumber α becomes $O(Re^{-1})$ at which point the critical layer expands to fill the domain (Deguchi, Hall & Walton 2013). Stable stratification, however, causes this regime to be realised for $\alpha = O(1)$ when $Ri_b \sim Re^{-2/3}$. The effect of both spanwise and cross-stream localisation of the flow is to reduce the regions where the flow is directed against gravity and hence to keep the potential energy low. In fact, E_p stays $O(Re^{-2})$ as in regime 1 and remains comparable to E_k^v when $Ri_b = O(Re^{-2/3})$.

The right hand side plot in figure 20 shows that plotting $Re^{2/3}\Delta$ verses $Re^{2/3}Ri_b$ does a good job of collapsing the data for $Re \in [10,000, 80,000]$ as far as Ri_b^{min} is concerned, i.e. the region around the stress deviation minimum. The collapse, however, is not compelling near Ri_b^{max} and suggests the presence of a third regime valid for $Ri_b \gg Re^{-2/3}$. Figure 18 gives some tentative evidence for this - see the transition from $Ri_b^{min}(40,000)$ (bottom left plot) to $Ri_b^{max}(40,000)$ (bottom right) - and Ri_b^{max} does not appear to be scaling with $Re^{-2/3}$ unlike Ri_b^{min} (see figure 21(d)). When $Ri_b \gg Re^{-2/3}$, a *further* rescaling of the vertical momentum equation (3.40) is required to balance the increased buoyancy term. Specifically,

$$(\partial_x, \partial_Y, \partial_Z) \to (\partial_x/\delta^*, \partial_Y/\varepsilon, \partial_Z/\varepsilon) \quad \text{and} \quad (U, V, W, R) \to (\varepsilon U, V/\varepsilon, W/\varepsilon, \varepsilon R) \tag{3.48}$$

where balancing advective, diffusive and buoyancy terms requires

$$\varepsilon = Ri_b^{-1/4} Re^{-1/6}, \quad \& \quad \delta^* = Ri_b^{-3/4} Re^{-1/2}. \tag{3.49}$$

This represents a *total* rescaling of

$$(\partial_x, \partial_y, \partial_z) \to (Ri_b^{3/4} Re^{1/2} \partial_x, Ri_b^{1/4} Re^{1/2} [\partial_y, \partial_z]) \quad \& \tag{3.50}$$

$$(u, v, w, \rho) \to Ri_b^{-1/4} Re^{1/2} (u, v, w, \rho). \tag{3.51}$$

When $Ri_b = O(1)$, the length scales in x, y and z become comparable and streamwise diffusion must be reintroduced. At this point, all terms in the momentum equation are important and the local Reynolds number is 1 (Deguchi (2015) calls this the 'Unit Reynolds number Navier-Stokes equations' or UNS regime). Explicitly, rescaling the total fields as

follows

$$(\partial_x, \partial_y, \partial_z) \to Re^{1/2}(\partial_x, \partial_y, \partial_z) \quad \text{and} \quad (u, v, w, \rho, p) \to (Re^{-1/2}[u, v, w, \rho], Re^{-1}p) \tag{3.52}$$

converts the Boussinesq equations (3.1)-(3.5) to

$$u_t + uu_x + vu_y + wu_z + p_x = \nabla^2 u, \tag{3.53}$$

$$v_t + uv_x + vv_y + wv_z + p_y = \nabla^2 v - Ri_b\, \rho \cos\theta, \tag{3.54}$$

$$w_t + uw_x + vw_y + ww_z + p_z = \nabla^2 w - Ri_b\, \rho \sin\theta, \tag{3.55}$$

$$\rho_t + u\rho_x + v\rho_y + w\rho_z = \frac{1}{Pr}\nabla^2 \rho, \tag{3.56}$$

$$u_x + v_y + w_z = 0. \tag{3.57}$$

where now asymptotic boundary conditions $(u, v, w, \rho) \to (\pm y, 0, 0, \mp y)$ as $y \to \pm\infty$ should be imposed. In this regime, the viscous diffusion time, the advective (turnover) time and the buoyancy timescale are all the same since the local Richardson number (which is the same as Ri_b here) is $O(1)$. Assuming the dissipation rate has a laminar scaling, $\Phi = O(1/Re)$, this corresponds to the statement that the $O(Re^{-1/2})$ lengthscale of the flow corresponds to both the Kolmogorov lengthscale $(\Phi Re^3)^{-1/4}$ and the Osmidov lengthscale $(\Phi Ri_b^{-3/2})^{1/2}$ and therefore is minimal i.e. the equations cannot support a smaller scale. This third regime then seems the ultimate regime as increasing Ri_b above $O(1)$ would lead to a stabilizing buoyancy force which could not be overcome by rescaling further: the solutions would simply cease to exist.

Since this third regime has localisation in all three directions, it presents a considerable numerical challenge to reach. Of the numerical solutions obtained, the streamwise gradients appear to stay $O(1)$ even at $Re = 80,000$ compared to the spanwise and cross-stream gradients: see figure 21 which plots $\hat{u}Re^{1/3}$ over the three directions for $Re = 10,000, 20,000, 40,000$ and $80,000$ at $Ri_b^{max}(Re)$. The localization length scale of $O(Re^{-1/3})$ is well established in the y (cross-stream) and z (spanwise) directions whereas the profiles in the x (streamwise) direction show no tendency to steepen with increasing Re. One strategy adopted by Deguchi (2017) to reach this regime is to force the flow to develop steep streamwise gradients by shrinking the computational box. The flow necessarily stays strictly periodic in both spanwise and streamwise directions as opposed to showing localisation but some evidence of this third regime can nevertheless then be found: see figure 4 of Deguchi (2017).

4. Discussion

We first summarise the findings of the paper which has considered stratified plane Couette flow where a stable density gradient is applied via Dirichlet boundary conditions on the flow.

(*a*) **Laminar-turbulent boundary.** Stratification increases the number of non-dimen -sional parameters specifying the system from 1 (Re) to 3 (Re, Ri_b, Pr). Reducing this to 2 by setting $Pr = 1$ throughout, a rough characterisation $Ri_b^c(Re)$ of the laminar-turbulent boundary in parameter space - the (Re, Ri_b) plane - has been made which shows that Ri_b^c is a monotonically increasing function of Re for $Re \leq 5000$. Of the two geometries considered, the larger computational box allows turbulence to reach slightly higher values of Ri_b^c at a given Re. Approaching this boundary by decreasing Re at small fixed Ri_b leads to the same situation as in unstratified where the turbulent attractor eventually collides with the laminar-turbulent boundary in *phase* space. In contrast

when the laminar-turbulent boundary is approach in *parameter* space by fixing Re and increasing Ri_b, the turbulent attractor expands displaying larger and larger fluctuations until ultimately it touches the laminar-turbulent boundary in *phase* space.

(*b*) **Edge-Tracking and ECS.** In order to understand this laminar-turbulent boundary, ECS were sought which exist beyond this (at higher Ri_b) in the (Re, Ri_b) plane. Edge tracking was performed for two reasons: 1) to select relevant ECS (otherwise unstratified states would have to be selected arbitrarily to continue to $Ri_b \neq 0$); and 2) to possibly find new states of non-SSP/VWI type. Despite investigating a number of different geometries, various parameter settings of Re and Ri_b, and combinations of imposed symmetries, only two simple states were found as edge states (the rest being chaotic). These states when continued back to $Ri_b = 0$ turned out to be EQ7 and EQ7-1 of Gibson & Brand (2014). No new states of non-SSP/VWI were found.

(*c*) **Connections with 2D convective roll solutions.**. Continuing EQ7-1, which is spanwise-localised at $Ri_b = 0$, to unstable stratifications ($Ri_b < 0$) revealed an interestingly simple delocalisation process whereupon the exponentially decaying tails gradually reduce their spatial decay rate to zero at a bifurcation point off a (spanwise global) 2D convective roll branch of solutions. EQ7 was similarly tracked back to a bifurcation off a (double layer) of 2D convective rolls as was Nagata's (1990) solution (confirming Clever & Busse (1992, 2000)).

(*d*) **Strong influence of stable stratification.** Continuing these solutions to $Ri_b > 0$ showed that stable stratification has a surprisingly strong effect on the SSP/VWI mechanisms. A simple connection between upper and lower EQ7 branches traced by allowing Ri_b to change continuously for $Re \leq 400$ is broken by $Re = 500$ revealing another branch of states which apparently give rise to new unstratified solutions (see figure 15). The lower branch of EQ7 solutions suffers a further topological change by $Re = 850$ so that the solutions for $Ri_b > 0$ become increasingly convoluted. Nagata's solution is also found to bifurcate off EQ7 for non-zero stable stratification.

(*e*) **Asymptotics.** Calculations for low Re (≤ 1000) indicate that EQ7 of the three types of solutions considered could survive to the highest levels of stratification. High Re (up to $80,000$) calculations were then done for EQ7 which revealed two regimes and hinted at a third. The first regime is characterised by $Ri_b = O(Re^{-2})$ - or Rayleigh number $Ra := -Ri_b Re^2 Pr = O(1)$ - where the SSP/VWI process underpinning EQ7 starts to feel the stratification. For $Ri_b \gg Re^{-2}$, EQ7 progressively localises in both the spanwise and cross-stream directions until at $Ri_b = O(Re^{-2/3})$, the localisation is on the scale of the critical layer. This signals the second regime where the asymptotic structure is described by a stratified version of the Boundary Reduced Equations of (Deguchi, Hall & Walton 2013; Deguchi & Hall 2015). For even larger Ri_b, the stabilising buoyancy force can be counterbalanced by further localisation which now has to include streamwise localisation until an ultimate third regime where $Ri_b = 0(1)$ appears possible. Here the scale of the flow in all three directions is simultaneously the minimal Kolmogorov scale and the Osmidov lengthscale, i.e. viscous, advective and buoyancy timescales all match. Numerical solutions indicate a transition out of the second regime but could not capture the third regime due to resolution issues.

One of the main findings of this work is that stable stratification has such a strong effect on the finite-amplitude states considered here. Bulk Richardson numbers of $O(Re^{-2})$ (actually an O(1) Rayleigh number for $Pr = O(1)$) are already enough to start modifying the SSP/VWI process which underpins all known ECS in pCf. To put this into some context, consider flow along a pipe of diameter D across which a temperature difference of δT is unwittingly applied. One can expect this temperature difference to have a significant effect on, say, measured wall stresses or phase speeds of ECS if $Ri_b Re^2 = -Ra/Pr = 10^3$

(see Appendix B and figure 20) where $Ra := \alpha g \delta T D^3/\nu^2$. Using the volumetric coefficient of thermal expansion for water at 20^oC, $\alpha = 2 \times 10^{-4}/K$, $g = 9.8\text{ms}^{-2}$, $D = 0.02\text{m}$ and $\nu = 10^{-6}\text{m}^2\text{s}^{-1}$ gives a $\delta T = 6.4 \times 10^{-2} K$ which is not particularly large (of course this would have to be applied consistently along the pipe and the fluid present in the pipe long enough to feel the imposed temperature difference).

Increasing the stratification further causes the ECS to progressively localise to reduce the potential energy penalty for vertical motions imposed by stable stratification. This occurs firstly in the spanwise and cross-stream directions and then in all three directions when $Ri_b \gg Re^{-2/3}$. Ultimately, the scale of localisation becomes the minimal possible in all three directions at $Ri_b = O(1)$ for large Re. The idealised plane Couette flow set-up analysed here of course imposes a specific shear and a density gradient through the boundary conditions. In more general flow conditions, the local shear and density gradient as measured by a gradient Richardson number Ri will vary so that a hierarchy of ECS with different length scales can exist in the same flow. The general conclusion of this work is that the smaller the lengthscale of the ECS the larger the local Ri which can be accommodated. For example, large scale flows can only accommodate $Ri = O(Re^{-2})$ levels of stratification whereas ECS on the scale of the Kolmogorov length can survive even when $Ri = O(1)$. The existence of these latter localised states means that there is no reason to doubt that stratified turbulence couldn't be present at $Ri_b = O(1)$ as $Re \to \infty$. Confirming this scenario is an important future challenge.

A question which has been left unanswered by this study is the possible existence of new types of finite-amplitude states which have no counterpart in the unstratified situation. Probing this issue would appear to require O(1) Richardson numbers (so the timescale of internal gravity waves match the advective timescale) which it is now clear requires large Re certainly beyond what has been studied numerically here. This and the issue of how the Prandtl number affects the solutions found here are important questions for future study.

Finally, it is interesting but perhaps not surprising that all of the three ECS studied here can be traced back to bifurcations off (primary) 2D convective roll solutions in sheared Rayleigh-Benard convection. Given that 2D finite amplitude rolls in sheared Rayleigh-Benard convection are essentially the same as in unsheared Rayleigh-Benard convection (e.g. the shear only acts to remove the degeneracy in the bifurcating roll orientation having no effect on the bifurcation point itself - Kelly (1977)), it is hard not to speculate that *all* ECS in *unstratified* pCf are actually borne in bifurcations which can be traced back to the linear instability problem in Rayleigh-Benard convection.

Acknowledgements After this work was submitted, we became aware of a closely related study by Deguchi (2017). The authors thank him for sharing his preprint. DO would like to thank CONACYT for the award of a scholarship which has supported his PhD studies and the availability of free HPC time on the University of Bristol's BlueCrystal supercomputer. Both DO and RRK thank the MUST team at Cambridge (Colm Caulfield, Stuart Dalziel, Paul Linden and John Taylor amonst others) for stimulating conversations and their interest in this work. RRK would also like to thank Paul Linden for asking about temperature effects in pipe flow.

Appendix A

A direct Newton-Raphson solver was used to track EQ7 around in parameter space. The velocity representation for a highly symmetric (i.e. possesses $\mathcal{S}$, Ω and $\mathcal{Z}$ symmetries) steady structure is

$$\begin{bmatrix} u \\ v \\ w \\ p \\ \rho \end{bmatrix} = \begin{bmatrix} y \\ 0 \\ 0 \\ 0 \\ -y \end{bmatrix} + \sum_{n=1}^{N} \sum_{\substack{m,\ell=0, \\ m+\ell \text{ even}}}^{M,L} \begin{bmatrix} (\,u^{(r)}_{nm\ell}\Phi_o(y) + iu^{(i)}_{nml}\Phi_e(y)\,)\cos\ell\beta z \\ (\,v^{(r)}_{nm\ell}\Phi_o(y) + iv^{(i)}_{nml}\Phi_e(y)\,)\cos\ell\beta z \\ (\,w^{(r)}_{nm\ell}\Phi_o(y) + iw^{(i)}_{nml}\Phi_e(y)\,)\sin\ell\beta z \\ (\,p^{(r)}_{nm\ell}\Psi_e(y) + ip^{(i)}_{nml}\Psi_o(y)\,)\cos\ell\beta z \\ (\,\rho^{(r)}_{nm\ell}\Phi_o(y) + i\rho^{(i)}_{nml}\Phi_e(y)\,)\cos\ell\beta z \end{bmatrix} e^{im\alpha x} + c.c.$$

The cross-stream basis functions Φ_e, Ψ_e (even in y) and Φ_o, Ψ_o (odd in y) were defined in two ways depending on whether one (Code 1) or two spectral elements (Code 2) were used. In Code 1,

$$[\,\Phi_o(y), \Phi_e(y)\,] := [\,T_{2n+1}(y) - T_{2n-1}(y),\ T_{2n}(y) - T_{2n-2}(y)\,],$$
$$[\,\Psi_o(y), \Psi_e(y)\,] := [\,T_{2n-1}(y),\ T_{2n-2}(y)\,]$$

with Dirichlet boundary conditions built into the bases Φ_e and Φ_o. The equations then only needed to be collocated over half the domain so the points

$$-1 < y_j := \cos\left[\frac{\pi(2(j+N)-1)}{4N}\right] < 0 \qquad j = 1...N \tag{4.1}$$

were used. In Code 2, the half interval $[-1, 0]$ was split into two domains $[-1, y_p]$ and $[y_p, 0]$ where y_p typically was chosen as -0.1 or -0.2. Then the following definitions were made

$$[\,\Phi_o(y), \Phi_e(y)\,] := \begin{cases} [\,T_{2n-1}(-y/y_p),\ T_{2n-2}(-y/y_p)\,] & y_p < y < 0 \\ [\,T_n(\overline{y}) + T_{n-1}(\overline{y}),\ T_n(\overline{y}) + T_{n-1}(\overline{y})\,] & -1 < y < y_p \end{cases}$$
$$[\,\Psi_o(y), \Psi_e(y)\,] := \begin{cases} [\,T_{2n-1}(-y/y_p),\ T_{2n-2}(-y/y_p)\,] & y_p < y < 0 \\ [\,T_{n-1}(\overline{y}),\ T_{n-1}(\overline{y})\,] & -1 < y < y_p \end{cases}$$

where $\overline{y} := (2y - y_p + 1)/(1 + y_p)$ (again Φ_o and Φ_e incorporate the Dirichlet boundary conditions) and collocation performed over the following points

$$y_j := \begin{cases} -y_p \cos\left[\frac{\pi(2(j+N_p)-1)}{4N_p}\right] & j = 1...N_p \\ \frac{1}{2}(y_p+1)\cos\left[\frac{\pi(2(j-N_p)-1)}{2(N-N_p)}\right] + \frac{1}{2}(y_p-1) & j = N_p+1...N. \end{cases} \tag{4.2}$$

Continuity of the zeroth and first derivatives of all the variables $[u, v, w, p, \rho]$ was then imposed at $y = y_p$ to match the spectral representations in the two domains (replacing the $j = N_p$ and $N_p + 1$ collocated equation constraints). The choice $N - N_p = 2N_p$ balances the spectral orders in the two domains and seemed to offer the best compromise between resolving the mid-plane area and allowing effective matching at $y = y_p$.

In code 1, the resolution near the mid plane is $\approx 1/2N$ whereas in code 2 it is $\approx |y_p|/2N_p$ which is $\approx 3|y_p|/2N$ if the choice $N - N_p = 2N_p$ is made. Choosing $y_p = -0.1$ therefore increases the mid plane resolution by a factor of over 3 for the same choice of N. Multithreaded OPENBLAS libraries allowed large resolutions to be handled. Typically, up to 125,000 degrees of freedom (requiring ≤ 128 GB of storage) were used - e.g. $(M, N, L) = (6, 100, 30)$ or $(10, 50, 20)$ - with some runs performed using close to 175,000 degrees of freedom (and up to 256 GB storage) - e.g. $(M, N, L) = (6, 140, 35)$ or $(18, 75, 24)$.

Appendix B

In the normal Rayleigh-Benard set-up (e.g. Drazin & Reid (1981) equations (8.6)-(8.8) with nonlinearities reinstated) the fully nonlinear equations for the total flow field $\mathbf{U}$ and temperature field Θ are

$$\frac{\partial \mathbf{U}}{\partial \tau} + \mathbf{U}\cdot\nabla\mathbf{U} = -\nabla P + Ra\,Pr\,\Theta\,\hat{y} + Pr\nabla^2\mathbf{U} \tag{4.1}$$

$$\frac{\partial \Theta}{\partial \tau} + \mathbf{U}\cdot\nabla\Theta = \nabla^2\Theta \tag{4.2}$$

$$\nabla\cdot\mathbf{U} = 0 \tag{4.3}$$

subject to boundary conditions

$$u(x,\pm 1,z,t)) = \pm 1 \quad \& \quad \theta(x,\pm 1,z,t) = \mp 1. \tag{4.4}$$

Stratified plane Couette flow (as described by equations (2.1)-(2.3)) is retrieved under the following transformation

$$t = (RePr)\tau, \quad \mathbf{u} = \mathbf{U}/(RePr), \quad \rho = \Theta, \quad p = P/(RePr)^2 \tag{4.5}$$

so that $Ra = -Ri_b\,Re^2\,Pr$. The critical Ra for linear instability is $Ra_{crit} := 1708/16$ which is unchanged by introducing a unidirectional shear (e.g. Kelly (1977))†.

The critical Re for energy stability, Re_{ES}, for this system is as follows (Joseph 1966)

$$Re_{ES} = \begin{cases} \frac{1}{2}\sqrt{1708} & Ri_b > 0, \\ \frac{1}{2}\sqrt{1708}/\sqrt{1+4Pr(-Ri_b)} & Ri_b < 0 \end{cases} \tag{4.6}$$

Alternatively, the Rayleigh-Benard problem with shear has an energy stability threshold, Ra_{ES}, given by

$$Ra_{ES} = Ra_{crit} - \tfrac{1}{4}Re^2 \tag{4.7}$$

so $Ra_{ES} = Ra_{crit}$ *only* for no shear.

REFERENCES

Armenio, V. and Sarkar, S. 2002 "An investigation of stably stratified turbulent channel flow using large-eddy simulation" *J. Fluid Mech.* **449**, 1-42.

Blackburn, H. M., Hall, P. and Sherwin, S. J. 2013 "Lower branch equilibria in Couette flow: the emergence of canonical states for arbitrary shear flows" *J. Fluid Mech.* **726**, R2.

Clever, R. M., Busse, F. H. and Kelly, R. E. 1977 "Instabilities of longitudinal convection rolls in couette flow" *ZAMP* **28**, 771-783.

Clever, R. M. and Busse, F. H. 1992 "3-Dimensional convection in a horizontal fluid layer subjected to a constant shear" *J. Fluid Mech.* **234**, 511-527.

Chandler, G. J. and Kerswell, R. R. 2013 "Invariant recurrent solutions embedded in a turbulent two-dimensional Kolmogorov flow" *J. Fluid Mech.* **722**, 554-595.

Clever, R. M. and Busse, F. H. 2000 "Tertiary and quarternary solutions for plane Couette flow with thermal stratification" *Conference: 11th International Couette-Taylor Workshop Location: BREMEN, GERMANY Date: JUL 20-23, 1999 PHYSICS OF ROTATING FLUIDS Book Series: LECTURE NOTES IN PHYSICS* editors Egbers, C. and Pfister, G. **549**, 399-416.

Davey, A and Reid, W.H. 1977 "On the stability of stratified viscous plane Couette flow. Part 2. variable buoyancy frequency" *J. Fluid Mech.* **80**, 509-525.

Deguchi, K., Hall, P. and A. G. Walton 2013 "The emergence of localized vortex-wave interaction states in plane Couette flow" *J. Fluid Mech.* **721**, 58-85.

† The factor of 1/16 is because the half-channel width has been used to non-dimensionalize the system

Deguchi, K. and Hall, P. 2014 "Canonical exact coherent structures embedded in high Reynolds number flows" *Phi. Trans. R. Soc.* **372**, 20130352.

Deguchi, K. 2015 "Self-sustained states at Kolmogorov microscale" *J. Fluid Mech.* **781**, R6.

Deguchi, K. 2017 "Scaling of small vortices in stably stratified shear flows" *J. Fluid Mech.* in press.

Deguchi, K. and Hall, P. 2015 "Asymptotic descriptions of oblique coherent structures in shear flows" *J. Fluid Mech.* **782**, 356-367.

Deusebio, E., Caulfield, C. P. and Taylor, J. R. 2015 "The intermittency boundary in stratified plane Couette flow" *J. Fluid Mech.* **781**, 298-329.

Drazin, P.G. and Reid, W.H. 1981 *Hydrodynamic Stability*, C.U.P., Cambridge.

Duguet, Y., Willis, A. P. and Kerswell, R. R. 2008 "Transition in pipe flow: the saddle structure on the boundary of turbulence" *J. Fluid Mech.* **613**, 255-274.

Duguet, Y., Brandt, L. and Larsson, B. R. 2010 "Towards minimal perturbations in transitional plane Couette flow" *Phys. Rev. E* **82**, 026316.

Eaves, T. S. and Caulfield, C. P. 2015 "Disruption of SSP/VWI states by stable stratification" *J. Fluid Mech.* **784**, 548-564.

Eckhardt, B., Schneider, T. M., Hof, B. and Westerweel, J. 2007 "Turbulence transition in pipe flow" *Ann. Rev. Fluid Mech.* **39**, 447-468.

Faisst, H. and Eckhardt, B. 2003 "Travelling waves in pipe flow" *Phys. Rev. Lett.* **91**, 224502.

Garcia-Villalba, M. and del Alamo, J.C. 2011 "Turbulence modification by stable stratification in channel flow" *Phys. Fluids*, **23**, 045104.

Gibson, J. F., Halcrow, J. and Cvitanović, P. 2008 "Visualizing the geometry of state space in plane Couette flow" *J. Fluid Mech.* **611**, 107-130.

Gibson, J. F., Halcrow, J. and Cvitanović, P. 2009 "Equilibrium and travelling-wave solutions of plane Couette flow" *J. Fluid Mech.* **638**, 243-266.

Gibson, J. F. and Cvitanović, P. 2010 "Geometry of the turbulence in wall-bounded shear flows: periodic orbits" *Physica Scripta* **142**, 014007.

Gibson, J. F. and Brand, E. 2014 "Spanwise-localized solutions of planar shear flows" *J. Fluid Mech.* **745**, 25-61.

Generalis, S. and Nagata, M. 2003 "Transition in homogeneously heated inclined plane parallel shear flows" *J. Heat Trans.* **125**, 795-803.

Hall, P. and Smith, F. T. 1991 "On strongly nonlinear vortex/wave interactions in boundary-layer transition" *J. Fluid Mech.* **227**, 641-666.

Hall, P. and Sherwin, S. 2010 "Streamwise vortices in shear flows: harbingers of transition and the skeleton of coherent strctures" *J. Fluid Mech.* **661**, 178-205.

Hall, P. 2012 "Vortex-wave interactions/self-sustained processes in high Prandtl number natural convection in a vertical channel with moving sidewalls" *Stud. Appl. Math.* **129**, 1-25.

Hof, B., van Doorne, C. W. H., Westerweel, J., Nieuwstadt, F. T. M., Faisst, H., Eckhardt, B., Wedin, H., Kerswell, R.R. and Waleffe, F. 2004 "Experimental observation of nonlinear travelling waves in turbulent pipe flow" *Science* **305**, 1594-1598.

Howard, L. N. and Maslowe, S. A. 1973 "Stability of stratified shear flows" *Boundary Layer Meteorology* **4**, 511-523.

Huppert 1973 "Howard's technique for perturbing neutral solutions of the Taylor-Goldstein equation" *J. Fluid Mech.* **57**, 361-368.

Itano, T. and Toh, S. 2001 "The dynamics of bursting process in wall turbulence" *J. Phys. Soc. Japan* **70**, 703-716.

Itano, T. and Generalis, S. C. 2009 "Hairpin vortex solution in planar Couette flow: a tapestry of knotted vortices" *Phys. Rev. Lett.* **102**, 114501.

Joseph, D. D. 1966 "Nonlinear stability of the Boussinesq equations by the method of energy" *Arch. Rat. Mech. Anal.* **22**, 163.

Kawahara, G. and Kida, S. 2001 "Periodic motion embedded in plane Couette turbulence: regeneration cycle and burst" *J. Fluid Mech.* **449**, 291-300.

Kawahara, G., Uhlmann, M. and van Veen, L. 2012 "The significance of simple invariant solutions in turbulent flows" *Ann. Rev. Fluid Mech.* **44**, 203-225.

Kelly, R. E. 1977 "The onset and development of Rayleigh-Benard convection in shear flows: a review" in *Physicochemical hydrodynamics* (D.B. Spaulding, ed.), Advance Publications, London, 65-79.

Kerswell, R. R. 2005 "Recent progress in understanding the transition to turbulence in a pipe" *Nonlinearity* **18**, R17-R44.

Kerswell, R. R. and Tutty, O. R. 2007 "Recurrence of travelling waves in transitional pipe flow" *J. Fluid Mech.* **584**, 69-102.

Lucas, D. and Kerswell, R. R. 2015 "Recurrent flow analysis in spatiotemporally chaotic 2-dimensional Kolmogorov flow" *Phys. Fluids* **27**, 045106.

Mellibovsky, F., Meseguer, A., Schneider, T. M. and Eckhardt, B. 2009 "Transition in localized pipe flow turbulene" *Phys. Rev. Lett.* **103**, 054502.

Nagata, M. 1990 "3-Dimensional finite-amplitude solutions in plane Couette flow - bifurcation from infinity" *J. Fluid Mech.* **217**, 519-527.

Olvera, D. and Kerswell, R. R. 2017 *in preparation*

Pringle, C. C. T., Willis, A. P. and Kerswell, R. R. 2012 "Minimal seeds for shear flow turbulence: using nonlinear transient growth to touch the edge of turbulence" *J. Fluid Mech.* **702**, 415-443.

Rabin, S. M. E., Caulfield, C. P. and Kerswell, R. R. 2012 "Triggering turbulence efficiently in plane Couette flow" *J. Fluid Mech.* **712**, 244-272.

Schneider, T. M., Eckhardt, B. and Yorke, J. A. 2007 "Turbulence transition and the edge of chaos in pipe flow" *Phys. Rev. Lett.* **99**, 034502.

Schneider, T. M., Gibson, J. F., Lagher, M., De Lillo, F. and Eckhardt, B. 2008 "Laminar-turbulent boundary in plane Couette flow" *Phys. Rev. E* **78**, 037301.

Schneider, T. M. and Eckhardt, B. 2009 "Edge states intermediate between laminar and turbulent dynamics in pipe flow" *Phil. Trans. Roy. Soc.* **1888**, 577-587.

Schneider, T. M., Gibson, T. M. and Burke, J. 2010a "Snakes and Ladders: Localized solutions in plane Couette flow" *Phys. Rev. Lett.* **104**, 104501.

Schneider, T. M., Marinc, D. and Eckhardt, B. 2010b "Localized edge states nucleate turbulence in extended plane Couette cells" *J. Fluid Mech.* **646**, 441-451.

Skufca, J. D., Yorke, J. A. and Eckhardt, B. 2006 "Edge of chaos in a parallel shear flow" *Phys. Rev. Lett.* **96**, 174101.

Taylor, J. R. 2008 "Numerical simulations of the stratified ocenaic bottom boundary layer" PhD thesis, Mechanical Engineering, University of California, San Diego. (see http://www.damtp.cam.ac.uk/user/jrt51/files.html for diablo).

Thorpe, S. A. 2007 "The Turbulent Ocean" Cambridge University Press, Cambridge, UK.

Viswanath, D. 2007 "Recurrent motions within plane Couette turbulence" *J. Fluid Mech.* **580**, 339-358.

Viswanath, D. and Cvitanović, P. 2009 "Stable manifolds and the transition to turbulence in pipe flow" *J. Fluid Mech.* **627**, 215-233.

Wang, J., Gibson, J. F. and Waleffe, F. 2007 "Lower branch coherent state: transition and control" *Phys. Rev. Lett.* **98**, 204501

Waleffe, F. 1995 "Hydrodynamic stability and turbulence - beyond transients to a slef-sustaining process" *Stud. Appl. Math.* **95**, 319-343.

Waleffe, F. 1997 "On a self-sustaining process in shear flows" *Phys. Fluids* **9**, 883-900.

Waleffe, F. 1998 "Three-dimensional coherent states in plane shear flows" *Phys. Rev. Lett.* **81**, 4140.

Wedin, H. and Kerswell, R. R. 2004 "Exact coherent structures in pipe flow: travelling wave solutions" *J. Fluid Mech.* **508**, 333-371.

Willis, A. P., Cvitanovic, P. and Avila, M. 2013 "Revealing the state space of turbulent pipe flow by symmetry reduction" *J. Fluid Mech.* **721**, 514-540.